Plk4 triggers autonomous de novo centriole biogenesis and maturation

Catarina Nabais[1], Delphine Pessoa[1#], Jorge de-Carvalho[1#], Thomas van Zanten[2], Paulo Duarte[1], Satyajit Mayor[2], Jorge Carneiro[1], Ivo A. Telley[1,§], and Mónica Bettencourt-Dias[1,§]

[#] equal contribution

[§] co-lead authors

Affiliations:

[1] Instituto Gulbenkian de Ciência (IGC), Rua da Quinta Grande, 6, 2780-156 Oeiras, Portugal.

[2] National Centre for Biological Sciences (NCBS), Bellary Road, Bangalore 560065, Karnataka, Bangalore, India.

Correspondence to:

catarina.p.nabais@gmail.com; itelley@igc.gulbenkian.pt; mdias@igc.gulbenkian.pt

Keywords: Centriole, de novo organelle biogenesis, Plk4, molecular switch, concentration threshold.

Running Title: Regulation of de novo centriole biogenesis.

Abstract

Centrioles form centrosomes and cilia. In most proliferating cells, centrioles assemble through canonical duplication, which is spatially, temporally and numerically regulated by the cell cycle and the presence of mature centrioles. However, in certain cell-types, centrioles assemble de novo, yet by poorly understood mechanisms. Here, we established a controlled system to investigate de novo centriole biogenesis, using *Drosophila melanogaster* egg explants overexpressing Polo-like kinase 4 (Plk4), a trigger for centriole biogenesis. At high Plk4 concentration, centrioles form de novo, mature and duplicate, independently of cell cycle progression and of the presence of other centrioles. We show that Plk4 concentration determines the kinetics of centriole assembly. Moreover, our results suggest Plk4 operates in a switch-like manner to control the onset of de novo centriole formation, and that distinct biochemical kinetics regulate de novo and canonical biogenesis. Finally, we investigated which other factors modulate de novo centriole assembly and reveal that PCM proteins promote biogenesis, likely by locally concentrating critical components.

Introduction

"(...) *the problem which has interested cytologists and embryologists for many years, namely, whether an ordinarily self-duplicating body may, under certain conditions, seem to be created de novo."* (Dirksen, 1961): On *The presence of centrioles in artificially activated sea urchin eggs.*

It was not long after their discovery in cells in the late 1890's (by Boveri and van Beneden), that scientists began proposing that centrioles were not always assembled through duplication (Harvey, 1936; Yatsu, 1905). The fascinating discovery that such an elaborate yet fully functional structure can form without a template, raised a variety of questions regarding the regulation of organelle biogenesis, many of which stay pertinent to this date. And while much effort has contributed to our current understanding of the regulation of pro-centriole assembly next to an already mature, mother structure, much less is known regarding the "unguided" de novo centriole formation.

Centrioles are cylindrical microtubule (MT)-based structures that assemble centrosomes and cilia in eukaryotic cells. The animal centrosome is typically composed of two centrioles, surrounded by Pericentriolar Material (PCM), a membrane-less compartment, which contains hundreds of proteins organised within distinct domains, that are responsible for anchoring and nucleating MTs (see (Joukov and Nicolo, 2019) for a thorough review).

Centriole biogenesis is usually tightly regulated to ensure a correct organelle copy number and prevent a variety of human diseases, including cancer and microcephaly (Bettencourt-Dias et al., 2011; Godinho and Pellman, 2014; Godinho et al., 2014; Levine et al., 2018; Marteil et al., 2018; Lopes et al., 2018). In proliferating cells, centriole biogenesis occurs through a canonical pathway synchronous with cell-cycle progression, called centriole duplication. Accordingly, centrioles begin assembling at G1-S transition, whereby a single procentriole forms at the proximal side of each of the two mother centrioles (reviewed in (Nigg and Holland, 2018; Breslow and Holland, 2019). During mitosis, centrioles undergo centriole-to-centrosome conversion through the recruitment of Cep135/Bld10, Cep295/Ana1 and Cep152/Asterless (Asl), becoming competent for duplication in the next cell-cycle (Fu et al., 2016; Izquierdo et al., 2014; Wang et al., 2011; Tsuchiya et al., 2016). After mitosis, one centrosome is segregated to each daughter cell. This process entails that the location, timing and number of procentrioles

assembled in cycling cells is determined by older/mature centrioles (Banterle and Gönczy, 2017; Breslow and Holland, 2019).

Polo-like kinase 4 (Plk4) is a major player in centriole biogenesis in most animal cells (Bettencourt-Dias et al., 2005; Habedanck et al., 2005; Kleylein-Sohn et al., 2007). Depletion or inhibition of its kinase activity prevents centriole formation, while overexpression leads to the formation of multiple centrioles (Bettencourt-Dias et al., 2005; Habedanck et al., 2005; Wong et al., 2015). Plk4 activity and function is regulated by its concentration, which is known to be very low in human cultured cells (Bauer et al., 2016). As a result, the concentration of active Plk4 must be well-regulated to maintain a correct centriole number and normal cell-cycle progression. Full Plk4 activity is accomplished by trans-autophosphorylation of a conserved T-loop residue within its catalytic domain, which triggers kinase activation through a positive feedback mechanism (Lopes et al., 2015). It is still not fully understood how Plk4 acquires basal catalytic activity, but it is likely that other centrosomal proteins regulate this process, such as its substrates Ana2 and Asl (Klebba et al., 2015b; a; Moyer et al., 2015; Zitouni et al., 2016; Mclamarrah et al., 2018; Boese et al., 2018; Aydogan et al., 2019). Moreover, at high concentration, Plk4 self-assembles into nanoscale condensates in *Xenopus* extracts and in human cultured cells, which may be important for centriole assembly (Montenegro Gouveia et al., 2018; Yamamoto and Kitagawa, 2019; Park et al., 2019).

Centrioles can also form de novo in a variety of cell-types (reviewed in (Nabais et al., 2018)), but the regulation of this process remains largely unknown. De novo centriole assembly occurs naturally in organisms that lack centrosomes and generate centrioles to nucleate motile cilia, such as land plants that produce ciliated sperm (Renzaglia and Garbary, 2001), several unicellular organisms that alternate between non-flagellated and flagellated life-cycle states and in animal multiciliated cells, where many centrioles are produced at once (Dingle and Fulton, 1966; Aldrich, 1967; Fulton and Dingle, 1971; Grimes, 1973a; b; Mir et al., 1984; Al Jord et al., 2014; Meunier and Azimzadeh, 2016; Fritz-Laylin et al., 2016; Mercey et al., 2019a; b; Zhao et al., 2019) Furthermore, centrosomes form de novo in parthenogenetic insects that develop without fertilisation (Riparbelli et al., 1998; Tram and Sullivan, 2000; Riparbelli and Callaini, 2003). In most animals, centrioles are lost during female oogenesis and are provided by the sperm upon fertilisation, as they are needed for embryo development (Rodrigues-martins et al., 2008; Varmark et al., 2007). However, *Nasonia vitripennis* and *Muscidifurax uniraptor* wasps (Riparbelli et al., 1998; Tram and Sullivan, 2000; Ferree et al., 2006), *Drosophila mercatorum* flies (Riparbelli and Callaini, 2003) and *Acyrthosiphon pisum* aphids (Riparbelli et al., 2005) can reproduce in the absence of fertilisation. In these cases,

multiple centrosomes form spontaneously in the egg at late stages of meiosis, two of which are captured for spindle formation and embryo development, thus replacing the centrioles that are otherwise inherited from the sperm (Tram and Sullivan, 2000).

Centrioles can also form de novo in cells that undergo physical, chemical or genetic perturbations. Proliferating cells are capable of assembling centrioles de novo, but only after their centrosomes have been physically or chemically removed (Khodjakov et al., 2002; La Terra et al., 2005; Uetake et al., 2007). *Chlamydomonas reinhardtii* carrying a mutated centrin copy has defects in centriole segregation giving rise to progeny without centrioles that, within few generations, reacquire centrioles de novo (Marshall et al., 2001). Although in these cases there is no strict control over the number of centrioles formed, it has been proposed that resident centrioles negatively regulate de novo centriole biogenesis (Marshall et al., 2001), and that such inhibitory effect can be accomplished by having a single centriole in the cell (La Terra et al., 2005; Lambrus et al., 2015).

In *Drosophila* tissue culture cells, evolutionary conserved centriolar components, such as Sas6, Sas4 and Bld10, are critical for both canonical and de novo assembly (Rodrigues-Martins et al., 2007), suggesting that centrioles assembled by both pathways share their core composition but perhaps differ in their triggering. Despite the wide spread circumstances in which centrioles form de novo, the regulation and role of older centrioles on this process have not been addressed. This is in part due to the lack of a controlled model system suitable for high-resolution time-lapse imaging and amenable to experimental perturbations.

In this study, we investigated the spatio-temporal regulation behind de novo centriole assembly, including the effect of pre-assembled centrioles on the biogenesis of new ones, by developing a new experimental system that enabled tracking this process visually. Plk4 upregulation drives de novo centriole biogenesis in unfertilised *Drosophila melanogaster* eggs (Rodrigues-Martins et al., 2007; Peel et al., 2007). The fly egg is ideal to study centriole assembly since all the proteins necessary for the first centrosome and nuclear cycles are maternally inherited and, in the absence of fertilisation, centrioles are not present. Therefore, centrosomes detected in unfertilised eggs result from de novo assembly and not from duplication from paternally inherited centrioles. Here, we accomplished, for the first time, fast live-imaging of de novo centriole assembly with high spatial resolution, using single-egg cytosolic explants (Telley et al., 2013; de-Carvalho et al., 2018). We show that, at high Plk4 concentration, centrioles form de novo and then become competent to duplicate, and that both pathways are concurrent. We present a

combination of experiments and mathematical modelling that reveal that de novo centriole formation occurs independent of pre-existing centrioles. These results contradict the existing view that resident centrioles generate signals that inhibit de novo biogenesis. We demonstrate that Plk4 modulates the kinetics of centriole assembly in a concentration-dependent manner that is suggestive of a switch-like molecular mechanism. Finally, we find that the PCM, in particular Gamma-tubulin, regulates de novo biogenesis, suggesting that a local environment of concentrated centriolar and PCM components is required for de novo centriole assembly.

Results

An assay to investigate centriole biogenesis live with high spatio-temporal resolution

De novo centriole assembly has remained poorly studied in live samples due to the lack of a suitable system where the process can be triggered and documented in a timely-manner. Overexpressing Polo-like kinase 4 (Plk4) drives de novo bona fide centriole biogenesis, validated by Electron Microscopy (EM), in unfertilised *Drosophila melanogaster* eggs (Rodrigues-Martins et al., 2007), but the onset of the process and its spatio-temporal dynamics was unknown. Reasons behind this knowledge gap are mostly imaging-related, for the axial depth is optically limited and greatly impaired by the light scattering properties of the egg yolk. Therefore, it is currently impossible to visualise events that take place deep inside the fruit-fly egg, which would otherwise be the ideal system to address critical questions concerning centriole biogenesis.

We set up a cell-free assay that resolves these limitations by generating cell cortex-free micro-scale explants that can be fully imaged, while retaining the native characteristics of the cytoplasm in vivo (Fig. 1A, (Telley et al., 2013; de-Carvalho et al., 2018). Using this assay, we observed de novo centriole biogenesis, at high spatio-temporal resolution (Fig. 1B,C and Suppl. Movie 1). Germline-specific Plk4 overexpression triggers the formation of multiple centrioles in cytoplasmic explants, demonstrating that post-meiotic *Drosophila melanogaster* egg extracts are competent for centriole biogenesis, recapitulating what we had previously observed in the egg (Fig. 1C; (Rodrigues-Martins et al., 2007). Therefore, these extracts offer a powerful assay to investigate the regulation of centriole assembly.

Centrosomes formed in the explants are stable at least within the first hour of the process, since we never observed centriole elimination during our time-lapse recordings. We tested several fluorescent protein fly lines in the explants, namely Ana1-Tomato, GFP-Plk4, Asl-mCherry, Spd2-GFP and Sas6-GFP. We chose Spd2-GFP as our routine centrosome reporter because its fluorescence signal was brighter and more photostable across explants than all the others tested. As a result, most experiments in this study were conducted using this protein reporter.

De novo formed centrioles mature and acquire the ability to duplicate in the absence of cell cycle progression

It was previously proposed that in both human cells (La Terra et al., 2005; Lambrus et al., 2015) and *Drosophila* eggs (Rodrigues-Martins et al., 2007), centrioles that form de novo can then duplicate in a canonical fashion. However, this was never confirmed directly and raises some questions; since centriole duplication is thought to depend on centriole maturation, a process called centriole-to-centrosome conversion (Wang et al., 2011; Izquierdo et al., 2014; Fu et al., 2016; Chang et al., 2016) and known to be coupled to cell cycle progression, which does not occur in eggs (Horner et al., 2006; Vardy and Orr-Weaver, 2007; Deneke et al., 2019). Thus, we first asked whether de novo formed centrioles can recruit Ana1 and Asterless (Asl), required for centriole-to-centrosome conversion, followed by the recruitment of Plk4 and *bona fide* centriole duplication (Fig. 2 and Suppl. Movies 2A–D). Surprisingly, we observed that recently born centrioles recruit signature molecules characteristic of centriole maturation, such as Ana1 (Fig. 2C) and Asl (Fig. 2D), in the absence of mitosis (Wang et al., 2011; Izquierdo et al., 2014; Fu et al., 2016; Chang et al., 2016). Moreover, the trigger of biogenesis, Plk4, is also recruited to the centrioles (Fig. 2A).

Next, we investigated whether centrioles that formed de novo also duplicate, as predicted by their ability to mature and recruit Plk4. In our assay, single centrioles are first detected as radially symmetrical intensity spots with Gaussian intensity profile (Fig. 2A,B,C, right). Over time, a single Spd2 Gaussian intensity profile can evolve into a mixture of at least two Gaussian distributions, consistent with the presence of more than one diffraction-limited centriole and canonical duplication (intensity line profiles in Fig. 2D). Since image resolution by conventional confocal microscopy is diffraction-limited, we proceeded to validate centriole duplication using higher resolution techniques. Validation by EM had previously been performed in intact eggs overexpressing Plk4, confirming the assembly of structurally normal centrioles (Rodrigues-Martins et al., 2007). Currently, it is not possible to accomplish EM validation in cytoplasmic droplets

since the egg explants are imbedded in halocarbon oil, which is not compatible with sample processing. Therefore, we resorted to 3D-Structured Illumination Microscopy (SIM), which has approximately twice the spatial resolution of confocal microscopy. Spd2–GFP visualised by 3D-SIM imaging forms a ring at the centre of the microtubule aster, with an inner diameter of about 230-320 nm when viewed in cross section (Suppl. Fig. 1, insets). Previous studies have demonstrated that Spd2 also forms toroids at the centrosome in *Drosophila* syncytial embryos, whereby Spd2 projections extend from a central hollow structure, which presumably contains a single centriole (Conduit et al., 2015). In addition, in our experiments smaller structures form adjacent to older centrioles which previously formed de novo, demonstrating the onset of canonical duplication is concomitant with de novo biogenesis in this system (Suppl. Fig. 1, Insets).

In 97% (66/68) of our time-lapse recordings captured by confocal microscopy, we observed the duplication of the first centriole within 2 to 3 minutes after its de novo assembly (Fig. 2D, scatter-plot). Finally, we asked whether centrioles are fully converting to centrosomes, maturing also in their ability to nucleate MTs. Indeed we observed that as they age, centrioles continue incorporating centrosomal proteins and increase their MTOC capacity, which is reported by the intensity of the microtubule-associated protein Jupiter (Fig. 2D, bottom).

Centriole-mediated regulation of centriole biogenesis

Interpretation of earlier experiments led to the model that existing centrioles play a dominant role in centriole assembly and negatively regulate de novo centriole biogenesis, and that this inhibitory effect can be accomplished by a single centriole in the cell (Marshall et al., 2001; La Terra et al., 2005; Uetake et al., 2007; Lambrus et al., 2015). Whether centrioles can release an inhibitory signal is unknown. On the other hand, it has been suggested that centrioles can act as catalysers of centriole biogenesis, by concentrating centriole components and therefore preventing biogenesis elsewhere (Marshall et al., 2001; Lopes et al., 2015).

We asked whether the appearance of the first centriole can prevent further de novo formation. Surprisingly, despite the assembly of centrioles and their duplication, we continue to see de novo formation (see timeline in Fig. 2D), challenging the view that existing centrioles have a context-independent inhibitory effect in centriole biogenesis. To further test this in more detail, we analysed the spatio-temporal regulation of de novo biogenesis, at high Plk4 concentration, by assessing if centrioles impact the place and timing of other de novo events (Fig. 3A, 4A and Suppl. Fig. 2). Once the first centrosome

had formed, we assessed if older centrioles affect the biogenesis of others, e.g. by promoting (triggering effect) or repressing (inhibitory effect) the assembly of new ones.

We did not observe a statistical difference in the pairwise inter-event distance between the first four centrioles formed de novo (Kruskal-Wallis mean rank test) (Fig. 3B, Suppl. Fig. 2). However, we noticed that new centrioles form, on average, more than 10 µm away from previous ones, regardless of centriole rank and droplet size (Fig. 3B,C), raising the question whether this process is spatially random and if there is any spatial regulation (e.g. an inhibitory effect) imposed by older centrioles on the birth of neighbours. To test these hypotheses we generated stochastic models with similar geometric constraints as the cytosolic explants, allowing us to compare observed and simulated data. By measuring the inter-event distances between four random events, independent and uniformly distributed within 3-dimensional spaces of similar geometry, we can derive that observations in explants do not significantly deviate from the random simulations (Fig. 3D). According to our measurements, older centrioles have only a short-range effect on the biogenesis of new centrioles, promoting canonical duplication in very close proximity, but not determining the place of de novo assembly elsewhere in the cytosol. Hence, on the scale of tens of micrometers centrioles behave as independent entities in the initial stages of de novo assembly. Our results strongly suggest that de novo centriole biogenesis is not affected by the mere presence of other centrioles. It is possible that biochemical changes at the level of the entire cytoplasm allow for stochastic de novo centriole formation. To obtain more insight we went on to study the temporal kinetics of de novo biogenesis.

The kinetics of de novo biogenesis

We measured the time for the first four de novo centrioles to appear in the explants (Fig. 4A). We detected, on average, a long lag-phase until the birth of the first de novo event, after which the process seemingly accelerated, presenting rates of de novo centriole biogenesis in the range of one every two minutes (Fig.s 4B). Assuming independent events with a constant rate, computer simulations predict that all inter-event times should follow a similar distribution. As depicted in Fig. 4C, not all of the observed inter-event distributions were within the confidence interval of the simulation. Moreover, the difference was more noticeable with higher number of centrioles (Fig. 4C). Maximum Likelihood Estimation of birth rate indicated a linear increase with centriole number (Fig. 4D). Altogether, our results demonstrate that the de novo centriole formation rate accelerates in time and may comprise two distinct phases. In an initial lag phase preceding the formation of the first centriole(s), the probability of centriole assembly is

very low. In the subsequent phase, most events seem to occur almost simultaneously. Such kinetics is reminiscent of a bistable process. Cell-cycle transitions typically show bistability; they rely on accumulation of a signal or activating enzyme, and the moment a critical transition occurs the kinetics becomes essentially irreversible and independent of the signal. This is true for the G2/M transition, which is driven by high Cdk1 activity. Low Cdk1-Cyclin B activity in interphase can drive S-phase onset and G2 progression, whereas high Cdk1-Cyclin B activity triggers mitotic entry. The difference between interphasic and mitotic Cdk activity likely relies on their concentration and phosphorylation thresholds required to activate substrates and drive the respective cell-cycle transition (Gutierrez-Escribano and Nurse, 2015; Swaffer et al., 2016; Godfrey et al., 2017). Here, we observe a burst in centriole biogenesis, after which all centrosomes are retained in the explants suggesting that the transition underlying their assembly is irreversible (Tyson and Novak, 2001; Charvin et al., 2009) We thus hypothesise that multiple foci centriole biogenesis are generated in the cytosol by the action of the bistable molecular switch arising from the stochastic Plk4 concentration and activity.

Plk4 concentration modulates the kinetics of centriole assembly

Little is known about the regulation of Plk4 activity and the onset of centriole biogenesis. Full Plk4 activity is accomplished by trans-autophosphorylation of a conserved T-loop residue within its catalytic domain, which triggers kinase activation through a positive feedback mechanism (Lopes et al., 2015). Consequently, the expected kinetics of Plk4 activation may greatly depend on local concentration and on overcoming a critical threshold (Fig. 5A). As found in other kinases, Plk4 possesses an autoinhibitory mechanism; once synthesised it is autoinhibited by a cis-interaction between its L1 linker and activation loop (T-Loop). Autoinhibition is relieved upon Plk4 homodimerisation through its Polo-box (PB) domain 3 and autophosphorylation of residues within L1 (Klebba et al., 2015a). Moreover, Plk4 binding to the substrate Stil/Ana2 increases Plk4 phosphorylation within its T-loop (Moyer et al., 2015; Zitouni et al., 2016). Therefore, Plk4 auto-phosphorylation and interaction with Stil may provide spatial and temporal regulation of Plk4 kinase activity in cells, activating Plk4 preferentially at the centrosome where it is concentrated. Moreover, Plk4 ability to form large order oligomers (“condensates”), may be important for the onset of centriole biogenesis (Montenegro Gouveia et al., 2018; Leda et al., 2018; Shohei and Kitagawa, 2018; Park et al., 2019). We hypothesised that, in the case Plk4-driven centriole biogenesis is based on a positive feedback mechanism, the initiation of biogenesis is concentration-dependent and relies on overcoming a critical, local threshold in kinase

activity (Fig. 5A). In addition, if the process is bistable, we expect the kinetics to remain fast once the critical transition has occurred, provided there is enough activator (Plk4) in the system. To test this, we established a titration assay for Plk4 concentration using egg cytoplasm. Wildtype eggs have all the components, except for Plk4, presumably at similar concentrations as Plk4–overexpressing eggs. Thus, mixing egg cytoplasm from these two genetic backgrounds dilutes only Plk4 within a range of full overexpression and endogenous levels. We measured the temporal kinetics of de novo centriole biogenesis for a series of dilutions. We found that all tested Plk4 dilutions – 0.5, 0.33 and 0.16 relative concentration – delay the onset of de novo centriole assembly (Fig. 5B). The delay is dilution dependent; centrosome formation occurs within all explants at the highest Plk4 concentration, saturating within 25 min. Saturation is not reached within the observation time at lower Plk4 concentrations, and the onset of de novo centriole assembly occurs progressively later with increasingly lower Plk4 concentration (Fig. 5C). Moreover, stochastic simulations taking into consideration Plk4 trans-auto-phosphorylation and dephosphorylation, were in agreement with most of the observed data (Suppl. Fig. 4). Our results suggest the presence of a concentration dependent Plk4 threshold, modulated by the activity of a putative counteracting phosphatase. As a consequence, the kinetics of Plk4 activity and centriole biogenesis is non-linear as previously hypothesised in Lopes et al. 2015. Our results also show that the time from the first to the second biogenesis event does not differ between high overexpression and dilutions (Fig. 5C, Suppl. Fig. 5), suggesting that Plk4-driven centriole assembly relies on such a switch-like molecular process. Our experiments provide the first evidence in vivo that Plk4 triggers de novo centriole biogenesis through a positive feedback mechanism marked by a critical threshold of Plk4 concentration.

Our results lead to the hypothesis that under endogenous conditions, Plk4 concentration in cells is very low and undergoes limited oligomerisation in the cytosol, which can prevent auto-activation until the sperm centriole enters the egg and locally concentrates Plk4. However, the concentration and the oligomerisation state of Plk4 in the cytoplasm have never been studied in *Drosophila*. Therefore, we decided to investigate these biochemical parameters in the early fly embryo using Fluorescence Correlation Spectroscopy (FCS).

Plk4 regulation under endogenous conditions

FCS is a technique with single molecule sensitivity, therefore ideal for quantification of low abundance proteins present at nanomolar to picomolar concentrations inside the cell. Previously, this technique has been used to determine the oligomerisation state of

another centriolar protein, Sas6, in human U2OS cells (Keller et al., 2014). Moreover, Plk1, also a member of the Polo-like kinase family, has been studied by FCS in human RPE1 cells (Mahen et al., 2011). FCS measurements revealed distinct diffusion coefficients for Plk1 in the cytoplasm, which correlated with its kinase activity during different cell-cycle stages (Mahen et al., 2011).

Therefore, we conducted in vivo FCS to determine Plk4 concentration, diffusion and oligomerisation in syncytial fly embryos in which Plk4 is at endogenous levels and both alleles were tagged with a fluorescent reporter by CRISPR (Suppl. Fig. 7 and Suppl. Movie 3). Despite the very low concentration, we could detect bursts of mNeonGreen–Plk4 fluorescence above background signal, which was assessed in control flies expressing only RFP-Tubulin (Suppl. Fig. 9A). More importantly, the mNeonGreen–Plk4 traces generated clear autocorrelation function (ACF) curves, whereas the background fluorescence measured in RFP–Tubulin expressing embryos did not autocorrelate (Suppl. Fig. 9B). For mNeonGreen–Plk4, the normalised ACF were best fitted, with minimal residuals, to a two-component diffusion model, and this fit was corroborated by the distribution obtained from the Maximum Entropy Method (MEM) fit (Fig. 6A, Suppl. Table 4). Two fractions of diffusing mNeonGreen–Plk4 were detected in the cytoplasm: one diffusing at 17.17 $\mu m^2/s$ which is similar to the fluorophore mNeonGreen alone (Suppl. Fig. 8D) and another, slower fraction diffusing at 1.49 $\mu m^2/s$ (Fig. 6A, Suppl. Table 4). While the first fraction probably refers to Plk4 monomers, the second cannot be explained by homo-oligomerisation alone, suggesting that a fraction of Plk4 may associate with quasi-immobile substrates in the cytosol.

Next, we calculated the total concentration of mNeonGreen–Plk4 in the cytosol and determined its oligomeric state using the brightness of injected mNeonGreen monomer as calibration (Suppl. Fig. 8). We confirmed that Plk4 concentration in the cytosol is very low, around 7.55 nM, and an estimate for diffusion in the cytosol suggests coexistence of monomeric and oligomeric form (Fig. 6B). More precisely, 30.1% of diffusing Plk4 is detected as a monomer, while around 69.9% forms low-order oligomers, likely dimers and at most tetramers (Fig. 6B). Altogether, the FCS results indicate that Plk4 is indeed a very low abundance protein that undergoes limited oligomerisation within the cytoplasm, in early-developing *Drosophila* embryos. Thus, the nanomolar concentration of Plk4 may be insufficient to trigger de novo centriole assembly.

The change in the kinetics of de novo centriole assembly in response to Plk4 concentration allied to the current body of knowledge in the centrosome field, collectively suggest that centriole formation is critically regulated by timely concentration of

centrosomal molecules in one single place (Rale et al., 2018; Takao et al., 2019). But what initiates the concentration of these centrosomal molecules? Recent studies suggest that the PCM may play an important role.

PCM components promote the early steps of centriole de novo assembly

In *D. melanogaster* cultured cells, co-depletion of the centriolar protein Ana2 and the PCM component D-Pericentrin–like protein (D-Plp) additively impair centriole biogenesis, indicating that two alternative pathways – a centriolar and a PCM-mediated – may be at play (Ito et al., 2019). Moreover, in mouse ependymal cells without centrioles and specialised electron-dense deuterosomes that can feed centriole assembly, a correct number of centrioles can form de novo within Pericentrin rich areas (Mercey et al., 2019b). To test the role of the PCM in de novo centriole assembly, we started by performing perturbation experiments in *Drosophila* DMEL cultured cells, since it is easier to knock down several genes in vitro than in the organism. To create an assay for de novo centriole assembly, we depleted centrioles through successive cell divisions in the presence of RNAi against Plk4. As cells proliferate in the absence of centriole duplication, centriole number is progressively reduced. This is followed by a recovery period, without RNAi against Plk4, where Plk4 translation is resumed and centrioles assemble de novo (Rodrigues-Martins et al., 2007).

After RNAi against Plk4, we further depleted PCM components, while allowing Plk4 translation to recover (Fig. 7A), which is sufficient to drive centriole de novo assembly in the mCherry (mCh)-treated control cells (Fig. 7B,C, and Suppl. Fig. 10). After 10 days, only 3% of the cells treated with RNAi against Plk4 had centrioles, whereas in the mCherry-treated control about 85% of the cells had at least one centriole, as expected (Rodrigues-Martins et al., 2007). Cells depleted of centrioles were then treated for four days with RNAi against PCM components including: Cnn + Asl + D-Plp + Spd2 together (referred to as “All PCM”), previously shown to be essential for PCM maintenance (Pimenta-Marques et al., 2016), and the downstream PCM protein, **γ**-tubulin, which is known to be important for MT nucleation across species and contribute for centriole duplication in *C. elegans* embryos and human cells (Dammermann et al., 2004; Kleylein-Sohn et al., 2007). While cells treated with control mCherry dsRNA recovered centriole number within 4 days after ceasing Plk4 dsRNA treatment (indicating that centrioles formed de novo), only 15-20% of the cells treated with dsRNA against “All PCM” had centrioles (Fig. 7C). Moreover, de novo centriole formation was impaired by **γ**-tubulin 23C depletion, whereby only 34–42% of Plk4 depleted cells recovered a normal centriole number (Fig. 7C, Suppl. Fig. 10). This result implies that Gamma-tubulin, a critical PCM

component necessary for microtubule nucleation at the centrosome, is important for de novo centriole biogenesis. We proceeded to validate this observation in vivo and generated fly lines expressing shRNA against Gamma-tubulin 23C and Gamma-tubulin 37C (a maternally expressed gene, mostly abundant in early fly development (Tavosanis et al., 1997), under control of the UASp/Gal4 system. Fertilised eggs laid by females overexpressing the shRNA targeting Gamma-tubulin 37C do not develop (Suppl. Table 7) and unfertilised eggs display spindle defects similar to those previously shown in oocytes from Gamma-tubulin 37C mutant females (yellow asterisks in Fig. 7D and in Suppl. Fig. 11) (Tavosanis et al., 1997), indicating this RNAi construct is likely functional. We collected unfertilised eggs expressing RNAi targeting Gamma-tubulin 23C and/or 37C, while simultaneously overexpressing Plk4, under control of the V32-Gal4 driver. In the control, centrioles form de novo in 73% (22/30) of the eggs overexpressing Plk4 alone (Fig. 7D,E and Suppl. Fig. 11). On the other hand, in the case of recombinant Gamma-tubulin 23C + 37C RNAi flies overexpressing Plk4, only 26% (14/54) of their eggs show centrioles, while individual Gamma-tubulin knock-downs display intermediate phenotypes (Fig. 7D,E and Suppl. Fig. 11). Therefore, Gamma-tubulin depletion seems to impair de novo centriole assembly in vivo too.

Discussion

De novo centriole assembly is widely documented across the eukaryotic tree of life. Numerous studies report its incidence and even its relationship with life-history traits in particular groups (Mizukami and Gall, 1966; Aldrich, 1967; Grimes, 1973a; b; Mir et al., 1984; Renzaglia and Garbary, 2001; Idei et al., 2013), but they have not addressed how de novo assembly is regulated in living cells and what the contribution of older centrioles to this process is. With the workflow here implemented, we demonstrate that cytosolic explants from post-meiotic *D. melanogaster* eggs overexpressing Plk4 are competent of centriole biogenesis, offering the opportunity to investigate centriole formation at high spatio-temporal resolution by confocal fluorescence microscopy (Fig. 1). In these explants, Plk4 triggers stochastic formation of multiple, stable centrioles. Our assay allowed us to study several important open questions regarding the regulation of de novo centriole biogenesis.

How is the timing of biogenesis regulated? Our current knowledge supports the need for extrinsic timely cues, provided by the cell cycle regulation, to control the centriole cycle (Wang et al., 2011; Izquierdo et al., 2014; Fu et al., 2016; Tsuchiya et al., 2016). However, here we observed that de novo formed centrioles can undergo time-

dependent centriole-to-centrosome conversion and maturation, incorporating Ana1, Asl, Spd2 and Plk4. Consequently, approximately 2–3 minutes after being born, centrioles nucleate more microtubules and can duplicate (Fig. 2, insets, Suppl. Fig. 1, insets). Given that unfertilised eggs are not progressing through the cell cycle (Horner et al., 2006; Vardy and Orr-Weaver, 2007; Deneke et al., 2019), our findings suggest that centriole de novo formation, maturation and duplication can occur even without cell cycle transitions, in particular without having to undergo mitosis. Surprisingly, we also observed that the duplication time is similar for the first centrosomes assembled de novo at high (undiluted) and lower (diluted) concentration of Plk4 (Suppl. Fig. 6). This indicates that, despite the absence of a typical cell-cycle "clock", canonical biogenesis is both spatially and temporally robust. Hence, we propose that distinct intrinsic "clocks" regulate de novo and canonical biogenesis, with de novo biogenesis being more sensitive to Plk4 concentration.

Our data suggests that a switch-like transition mediated by Plk4 activity occurs in the cytoplasm. Evidence for such molecular mechanism is supported by the change in the kinetics of de novo centriole biogenesis following the delay in assembly of the first de novo event, modulated by concentration of Plk4 (Fig. 4D, 5C and Suppl. Fig. 4). Theoretical modelling and simulations indicate that the rate of de novo centriole assembly accelerates with time, following the rise in Plk4 activity (Suppl. Fig. 6). The sensitivity to the dilutions of Plk4 expression agrees with the non-linear kinetics of Plk4 trans-autoactivation in the cytosol by Lopes et al. 2015, suggesting that the burst in biogenesis occurs once a critical activity threshold is overcome (also proposed by Lambrus et al. 2015 for the regulation of canonical duplication). Moreover, Plk4 may need to oligomerise to promote centriole assembly. Consistent with this we observe, oligomeric forms of Plk4 in the cytoplasm at extremely low concentrations of Plk4 (Fig. 6).

Centrosomal proteins are highly enriched in intrinsically disordered regions, coiled-coil domains and phosphorylation sites, which are critical for protein interactions and oligomerisation, therefore promoting assembly of protein scaffolds (Santos et al., 2013; Kuhn et al., 2014). For example, Sas6 self-assembly into homodimers is at the heart of the universal 9-fold symmetry (Nakazawa et al., 2007; Breugel et al., 2011; Kitagawa et al., 2011; Guichard et al., 2017). At high concentration, *Xenopus* Plk4 forms supramolecular scaffolds that bind other centrosomal proteins and nucleate MTs (Montenegro Gouveia et al., 2018). In human cells, the association of Plk4 into condensates was shown to be mediated by disordered regions within Plk4 (Yamamoto

and Kitagawa, 2019) and regulated by autophosphorylation (Montenegro Gouveia et al., 2018; Yamamoto and Kitagawa, 2019; Park et al., 2019).

In switch-like processes, critical thresholds exist that, whenever crossed, result in an irreversible transition. We suspect that the concentration of active Plk4 increases over time at multiple sites in the cytosol, overcoming the activity of counteracting factors and driving centriole biogenesis almost simultaneously in independent locations in the explants. We have demonstrated a concentration-dependent delay in the onset of de novo centriole biogenesis upon Plk4 dilution in wild-type extract (Fig. 5B), while the inter-event time is much less affected by the cytoplasmic dilutions (Fig. 5C, Suppl. Fig. 5) and the spatial dynamics still fall within random predictions at lower Plk4 overexpression (Suppl. Fig. 3). Our dilution experiments suggest that time-dependent localised concentration of Plk4 and, perhaps, association into higher-order structures drives de novo centriole biogenesis at multiple locations in the cytoplasm. Once a critical threshold in molecular concentration is locally crossed, Plk4-driven centriole assembly is irreversibly catalysed.

Which factors can help to locally increase the concentration of centriole components? Besides local Plk4 concentration, other factors may play a role in regulating the location of de novo centriole assembly. For instance, MTs likely participate to the localisation of some components at the centrosome through molecular motor based transport. Furthermore, the PCM was shown to be important for canonical centriole biogenesis (Dammermann et al., 2004; Pelletier et al., 2004; Kemp et al., 2004; Delattre et al., 2006; Kleylein-Sohn et al., 2007) and recent studies in multicilliated cells propose that, in the absence of centrioles or specialised deuterosomes, centrioles can form within PCM clouds (Mercey et al., 2019b). De novo centriole biogenesis has been described to occur within Pericentrin and Gamma-tubulin-rich foci in vertebrate somatic cells (Khodjakov et al., 2002). We have also hypothesised that, in our system, the early steps of de novo centriole assembly occur within a MT and PCM-rich environment. In agreement, our PCM perturbation experiments support an important role for the PCM, in particular its downstream component Gamma-tubulin, in de novo centriole assembly (Fig. 7, Suppl. Fig.s 10 and 11). The PCM may generate protein scaffolds in the cytoplasm where centriolar proteins bind with higher affinity, therefore locally concentrating these molecules and forming stable seeds for centriole biogenesis. Moreover, Gamma-tubulin promotes MT nucleation, which may attract more components via motor-based transport or through entrapment of proteins with MT-binding capacity, such as Plk4 (Montenegro Gouveia et al., 2018). These manifold properties of the PCM may promote centriole biogenesis within biochemically-confined environments in the cytoplasm.

Do centrioles influence the de novo assembly of others? Previous studies had suggested that once centrioles form de novo in cells without centrioles, any other events of biogenesis would be "templated", i.e., follow the canonical pathway (Marshall et al., 2001; La Terra et al., 2005; Uetake et al., 2007; Lambrus et al., 2015). This appears to be the case in *Naegleria gruberi*, where the first basal body assembles de novo but the second duplicates from the first (Fritz-Laylin et al., 2016), in acentriolar somatic human cells (La Terra et al., 2005; Uetake et al., 2007; Lambrus et al., 2015) and in green algae (Marshall et al., 2001). Together, these studies suggest that centrioles negatively regulate the de novo pathway and play a dominant role in biogenesis by recruiting the centrosomal components that limit biogenesis. In fly egg explants, we observed that centrioles continue to form de novo long after the first centriole has assembled and duplicated (Fig. 2). Both pathways – de novo formation and canonical duplication – co-occur within the same cytoplasmic compartment, indicating that "older" centrioles and their duplication do not prevent biochemically de novo centriole assembly, even at lower Plk4 overexpression (Fig. 5 and Suppl. Fig. 5). Thus, it appears that these pathways are not inherently mutually inhibitory in the fly germline.

We then wondered whether centriole assembly has a negative impact on the birth of other centrioles, for instance by changing the molecular composition of the cytoplasm. Addressing this problem required comparing our observations with random simulations results obtained under similar spatial geometries. This comparison strongly indicates that the first de novo events are spatially independent, suggesting that recently formed centrioles have only a very short-range effect, if any, on the biogenesis of new centrioles. They promote duplication at the centrosome but do not impact the place where new centrioles assemble de novo elsewhere in the cytosol (Fig. 3D and Suppl. Fig. 3). We cannot exclude the possibility that shortly after forming, centrioles are still immature and therefore incapable of inhibiting de novo biogenesis. However, this hypothesis seems unlikely given their ability to duplicate. Another explanation may be that the overall concentration of Plk4 in our system is so high that over-rides any possible spatial regulation, but our modelling suggests that the location of de novo centriole biogenesis remains random even at lower overall Plk4 concentration ("0.16", Suppl. Fig. 4). Our results provide further support that spatio-temporal (local) concentration of Plk4 must be well-regulated in cells to form an exact number of centrioles, since their presence is not necessarily enough to ensure centrioles can only form in the vicinity of existing ones.

How do our results fit with what naturally occurs in vivo and in nature? A previous study had estimated 1200–5000 Plk4 molecules per cell in asynchronous human cells, from which around 70 molecules are loaded at the centrosome (Bauer et

al., 2016). We generated flies labelled with mNeonGreen at Plk4 genomic loci by CRISPR (Suppl. Fig. 7) and confirmed that endogenous diffusing pool of Plk4 is present at very low concentration and undergoes limited self-association in the cytosol in early fly embryos (Fig. 6B). These properties of Plk4 in the cytosol are unfavourable for centriole de novo assembly, ensuring that centrioles form in the right place by canonical biogenesis. Our measurements help building a quantitative framework for the transition of Plk4 molecules from the cytoplasm to the centriolar compartment, which ultimately controls centriole biogenesis.

Finally, we wonder to what extent our findings in *D. melanogaster* relate to the naturally occurring parthenogenetic development in other organisms, including some species of wasps, flies and aphids (Riparbelli et al., 1998; Tram and Sullivan, 2000; Riparbelli and Callaini, 2003; Riparbelli et al., 2005; Ferree et al., 2006). In those cases, multiple functional centrosomes form spontaneously in the egg during meiosis, two of which assemble the first mitotic spindle and trigger normal development. In the case of *D. mercatorum*, the centrosomes that assemble *de novo* can also duplicate and they do so in a cell-cycle dependent manner (Riparbelli and Callaini, 2003). It would be relevant to determine if the burst in centrosome assembly coincides with an increase in global Plk4 concentration or activation in the egg of these species. Just like in our system, a highly variable number of MTOCs are assembled, suggesting the presence of a weak control mechanisms against de novo centriole formation in the germline, once the eggs enter meiosis. Further studies aimed at documenting centrosome birth dynamics and their maturation in these natural systems may find more about the principles that govern de novo centriole formation and their conservation throughout species evolution.

In oocytes from some parthenogenetic hymenoptera, maternal centrosomes form de novo close to cytoplasmic organelles highly enriched in Gamma-tubulin called accessory nuclei (Ferree et al., 2006). Moreover, centrosome ablation in vertebrate CHO cells is followed by accumulation of Gamma-tubulin and Pericentrin in nuclear-envelope invaginations, hours before bona-fide centrioles are detected (Khodjakov et al., 2002). Interestingly, if treated with nocodazole, acentriolar CHO cells are no longer capable of assembling centrioles de novo (Khodjakov et al., 2002). Therefore, our work besides substantiating previous studies, further suggests that the organisation of PCM-rich foci likely represent the first steps and are essential for de novo centriole assembly.

Despite a profound knowledge in the field concerning localisation and interaction of centrosomal molecules, and how these interactions change during the cell cycle, there is still a vast array of processes to uncover regarding the regulation of centriole assembly. For example, it remains important to investigate scaffold formation in vivo and how thresholds in activity of molecules affect formation, as these thresholds might also

598 regulate canonical centriole duplication and perhaps other critical transitions in organelle
599 assembly. It is yet unclear how PCM and MTs contribute to the early onset of centriole
600 formation. Understanding how these – activity threshold and sensitivity to them, as well
601 as PCM and MT-rich micro-environments – go awry may allow uncovering one putative
602 mechanism by which centriole number deregulation arises in human diseases, since an
603 increase in number of PCM-rich foci possibly promotes assembly of supernumerary
604 centrioles.
605
606

607 # Materials and Methods

608 ## Fly work and sample preparation

609 *D. melanogaster* stocks and husbandry

610 All *D. melanogaster* stocks used in this study are listed in Suppl. Table 1. Transgenic
611 mNeonGreen-Plk4 flies were generated in-house by CRISPR/Cas9-mediated gene
612 editing (Port et al., 2014). Twenty base-pairs guide RNAs (gRNA) targeting the N-
613 terminal region of Plk4, with 5' BbsI-compatible overhangs, were ordered as single-
614 stranded oligonucleotides (Sigma-Aldrich). The complementary oligonucleotides were
615 annealed, phosphorylated and cloned into BbsI-digested pCFD3-dU6:3gRNA
616 expression plasmid (from Simon Bullock, MRC, Cambridge, UK). A plasmid DNA was
617 designed for homologous recombination-mediated integration of mNeonGreen between
618 the 5´UTR and the first coding exon of Plk4. 1-kbp long 5' and 3' homology arms were
619 PCR-amplified from genomic DNA isolated from y1,M{nanos-Cas9.P}ZH-2A,w* flies
620 (Suppl. Table 2) (BDSC# 54591). The mNeonGreen coding sequence was PCR
621 amplified from plasmids (Suppl. Table 2). All fragments were sub-cloned into the pUC19
622 plasmid (Stratagene) using restriction enzymes: 5' Homology Arm - NdeI and EcoRI;
623 Fluorescent tag + linker - EcoRI and KpnI; 3' Homology Arm KpnI and XbaI. Synonymous
624 mutations were performed on the homology arms, removing the protospacer-adjacent
625 motif (PAM) sequence from the donor plasmid to prevent re-targeting. The final donor
626 template for homologous recombination-mediated integration was composed of a
627 fluorescent reporter and a short flexible linker (see sequence in Suppl. Table 2), flanked
628 by 1-kbp homology arms. Two circular plasmids – pCFD3-Plk4_gRNA and mNeonGreen
629 template – were co-injected into nos-Cas9 embryos (BDSC# 54591 (Port et al., 2014)).
630 Injected flies (F_0) were crossed to a balancer strain and single-fly crosses were
631 established from their offspring (F_1). The resulting F_2 generation was screened for

positive integrations by PCR, using primers dmPLK4 5UTR 3 FW and dmPLK4 1exon Rev (Suppl. Table 3). Homozygous mNeonGreen-Plk4 and pUb–RFP–β2-Tubulin flies (gift from Yoshihiro Inoue, (Kitazawa et al., 2014)) were crossed, establishing a stable stock.

We also generated flies expressing short hairpin RNAs (shRNA) against gamma-tubulin 37C and 23C under the UASp promoter and crossed them with the V32-Gal4 (w*; P{maternal-αtubulin4-GAL::VP16}V2H, kindly provided by Daniel St Johnston), at 25ºC, to knock-down both genes in the female germline. To generate gamma-tubulin 37C and 23C constructs, sense and antisense oligos for each target gene were annealed and cloned into pWALIUM22, using NheI and EcoRI restriction enzyme sites (Suppl. Table 6). Each construct was inserted into different landing sites on the third chromosome by PhiC31 integrase-mediated recombination (Suppl. Table 6). Germline-specific Plk4 overexpression was accomplished by crossing flies carrying the pUASp–Plk4 construct (Rodrigues-Martins 2007) and the V32-Gal4, at 25ºC.

Centrosomes were visualised using the following centrosomal reporters: i) pUb-Spd2–GFP (homemade construct, injected at BestGene Inc.); ii) Ana1–tdTomato (gift from Tomer Avidor-Reiss, (Blachon et al., 2008); iii) pUASp–GFP–Plk4 (homemade construct, injected at BestGene Inc.); iv) Asl-mCherry (gift from Jordan Raff, (Conduit et al., 2015)), in combination with either endogenous Jupiter–GFP (BDSC# 6836) or endogenous Jupiter–mCherry (gift from Daniel St Johnston, (Lowe et al., 2014)), as reporters for centrosomal microtubule nucleation.

Flies were maintained at 25ºC in vials supplemented with 20 mL of culture medium (8% molasses, 2.2% beet syrup, 8% cornmeal, 1.8% yeast, 1% soy flour, 0.8% agar, 0.8% propionic acid, and 0.08% nipagin).

Testing UASp-RNAi lines for developmental lethality

To test for lethality effects of γ-tubulin 37C and γ-tubulin 23C shRNAs alone and recombined, each line was crossed to V32-Gal4 flies. Female progeny carrying the Gal4 and shRNA was crossed to w^{1118} males (10 females x 5 males per vial, 4 independent crosses) and the number of pupae in each vial was counted 9-10 days after each transfer (3 technical repeats were performed). See results in Suppl. Table 7.

Embryo/Egg collections

For embryo collections, 3–4 days old female and male flies were transferred to a cage coupled to a small apple juice agar plate (25% apple juice, 2% sucrose, 1.95% agar and 0.1% nipagin), supplemented with fresh yeast paste. Embryos were collected for 1h and aged for half-an-hour. For unfertilised egg collections, around a hundred 5-7 days old virgin females were placed in the cage and 20 minutes collections were performed. All cages were maintained at 25ºC, under 50–60% humidity. The embryos or eggs were dechorionated in 7% Sodium Hypochlorite solution (VWR), washed thoroughly in milliQ water, aligned and immobilised on clean, PLL-functionalised coverslips, using a thin layer of heptane glue. Samples were covered with Voltalef grade H10S oil (Arkema).

Preparation of micropipettes and functionalised coverslips

High Precision 22x22 glass coverslips No 1.5 (Marienfeld) were cleaned for 10 min in 3M Sodium Hydroxide, followed by 4 dip-and-drain washes in milliQ water. Next, they were sonicated for 15 min in “Piranha” solution (H_2SO_4 and H_2O_2 (30% concentrated) mixed at 3:2 ratio), followed by two washes in MilliQ water, once in 96% ethanol and twice again in milliQ water for 5 min each. Coverslips were spin-dried and subsequently treated for 20 minutes with Poly-L-Lysine (PLL) solution 0.01 % (Sigma-Aldrich), followed by multiple dip-drain-washes in MilliQ water. The coverslips were spin-dried and stored in a clean and dry rack.

Glass capillaries (0.75mm inner diameter, 1 mm outer diameter; Sutter Instrument) were forged into glass needles by pulling them on a vertical pipette puller (Narishige PC-10), using a one-step pulling protocol, at about 55% heating power. Using a sharp scalpel, the tip of the capillary was cut, generating micropipettes with 30-35 µm diameter pointed aperture (Telley et al., 2013).

Single egg extract preparation

Cytoplasmic extraction from individual unfertilised eggs and explant deposition onto the surface of PLL-coated coverslips was performed on a custom-made micromanipulation setup coupled to an inverted confocal microscope, as previously described in (Telley et al., 2013) and (de-Carvalho et al., 2018). The size of the explants was manually controlled in order to produce droplets measuring between 40 - 80 µm in diameter and approximately 10 µm in height, allowing fast time-lapse imaging of the entire explant volume.

Egg immunostaining and imaging

Unfertilised eggs overexpressing Plk4 and knocked down for **γ**-tubulin were collected from 5–7 days old virgin females for 2h at 25ºC, and aged at 25ºC for 4 hours. Protocol was conducted according to (Riparbelli and Callaini, 2005). Briefly, aged eggs were rinsed in MilliQ water + 0.1% Tween, dechorionated in 7% Sodium Hypochlorite solution (VWR) and washed extensively with MilliQ water. Using a metal grid, dechorionated eggs were transferred into a scintillation flask containing 50% ice-cold Methanol + 50% Heptane. The vitelline membrane was removed by vigorously shaking the eggs for 3 min. Devitellinised eggs sunk to the bottom of the lower Methanol phase and were then collected into a 1.5 ml eppendorf and fixed for 10 minutes in Methanol at -20ºC. Following fixation, the eggs were rehydrated in Methanol:PBS series (70:30%, 50:50% and 30:70%) for 5 min each, washed twice in PBS for 10 min and incubated for 1 hour in D-PBSTB (1x Dulbecco's PBS, with 0.1% Triton X-100 and 1% BSA), at RT. Primary antibody incubations were performed overnight at 4ºC, with the following antibodies: rabbit anti-Bld10 (dilution 1:500; gift from Tim Megraw, The Florida State University, USA); rat anti-tubulin YL1/2 (dilution 1:50; Biorad) and guinea-pig anti-Ana1 (dilution 1:500; kindly provided by Jordan Raff), diluted in D-PBSTB. Eggs were washed extensively in D-PBSTB and incubated with secondary antibodies for 2h at RT - donkey anti-rabbit Alexa 555 (dilution 1:1000; Molecular Probes), goat anti-rat Alexa 488 (dilution 1:1000; Jackson Immunoresearch Laboratories) and donkey anti-guinea pig Alexa 647 (dilution 1:1000; Jackson Immunoresearch Laboratories) in D-PBSTB. Eggs were washed twice in PSB with 0.1% Triton X-100, twice in PBS and mounted onto coverslips in Vectashield mounting media (Vector Laboratories).

Imaging was conducted on a Nikon Eclipse Ti-E microscope equipped with a Yokogawa CSU-X1 Spinning Disk confocal scanner and a piezoelectric stage (Physik Instrumente) with 220 µm travel range. 0.3 µm optical sections were recorded with a EMCCD Photometrics 512 camera using a Plan Fluor 40x 1.30 NA oil immersion objective, controlled with Metamorph 7.5 software. 491 nm, 561 nm and 640 nm laser lines were used to excite the secondary antibodies. Egg counts were tested with a Chi-square test against the null-hypothesis that the outcome is random. Then, each test condition was compared to the control condition with a 2-proportions Z-test under H0 that the proportions of eggs with centrioles are equal versus HA that the proportion in the test is smaller. The significance level for multiple testing was Bonferroni corrected. Significance level was p=0.01.

Image acquisition, processing and analysis

730 Time-lapse explant imaging on the spinning disk confocal microscope

731 Centriole formation was followed by time-lapse imaging in droplets initially devoid of
732 centrosomes. Explants were imaged at room temperature using a Plan Apo VC 60x 1.2
733 NA water objective. 0.45 µm thick optical sections were acquired with an EMCCD Andor
734 iXon3 888 camera using a Yokogawa CSU-W1 Spinning Disk confocal scanner equipped
735 with a piezoelectric stage (737.2SL, Physik Instrumente), installed on a Nikon Eclipse Ti-
736 E microscope. Unless stated differently, dual-colour (488 nm and 561 nm excitation laser
737 lines), 15 seconds time-lapses of the explant volume were recorded with Andor IQ3
738 software.

739 Image processing

740 Multi-stack, time-lapse calibrated images were deconvolved with Huygens (Scientific
741 Volume Imaging, The Netherlands) using a Point Spread Function (PSF) automatically
742 calculated from the data set and run in batch mode, for each channel separately. 32-bit
743 deconvolved images were converted to 16-bit and processed using Fiji (NIH (Schindelin
744 et al., 2012)). Selected stills from the time-lapse acquisitions were processed with
745 Photoshop CS6 (Adobe). Graphic representations were performed using using
746 GraphPad Prism software (Version 5.0) and the final figures were assembled in Illustrator
747 CS6 (Adobe).

748 Centrosome tracking

749 Centrosomes were tracked using the Fiji Plug-in TrackMate v3.5.1 (Jaqaman et al.,
750 2008). Centrosomes were identified by the Spd2–GFP localisation at the centre of mass
751 of the microtubule aster. Relying on this criteria, we performed the TrackMate analysis
752 sequentially, starting with the Jupiter-mCherry channel. First, we applied a *3D Gaussian*
753 *Blur* filter to the images (sigma = 0.7 pixels), facilitating the particle detection on
754 TrackMate using the Laplacian of Gaussian algorithm. The microtubule asters were
755 automatically detected inside spheres of approximately 0.7 µm in radius, adjusting the
756 threshold value for each time-lapse video independently. Next, the first four de novo
757 formed asters were manually tracked from the list of detected particles. A corrected
758 XYZT coordinate matrix of the first de novo events was saved for each video and
759 imported to MatLab R2016b (The MathWorks, Inc.). MatLab was used to build a 3D
760 binary mask with spheres of radius *r* (where r ≥ microtubule aster size), centred at the
761 detected coordinate points. This allowed bypassing incorrect particle detection caused
762 by the large number of green auto-fluorescent yolk particles of intermediate signal

intensity, therefore excluding them from the analysis early on. The resulting 3D masks were concatenated into 4D hyperstacks, using the *Bio-Formats importer* plugin in FIJI. The Spd2–GFP images were multiplied by the corresponding 4D binary masks, resulting in a 4D image retaining the pixel intensity values solely within the Jupiter-mCherry ROIs. Next, we used *TrackMate* to detect centrioles within spheres of 0.3 µm radius, combining sub-pixel localisation and a *Median* filter. After detection, the particles were manually tracked. The final centrosome tracks were exported as an Excel MS spreadsheet.

Statistics and mathematical modelling

Centrosome tracking data was imported in R version 3.4.1 for further analysis and modelling. The data was analysed in two ways: one aiming at identifying possible spatial constraints in the positioning of the centrioles relative to each other within the droplet at the time a centrosome is formed (neglecting time), while the other aimed at understanding temporal constraints (neglecting space). The data was analysed statistically, and simulations were performed in an effort to understand the underlying principles. The details regarding sample size, statistical tests and descriptive statistics are indicated in the respective figure legends and in the main text.

The experimental data was compared to simulated data by calculating the empirical cumulative distributions of each dataset (one experimental and 100 simulated – each consisting of 68 droplets) using the function *ecdf* from the *stats* package; and overlapping the median and 95% confidence interval (from the quantiles 0.025 to 0.975) of the simulated datasets' cumulative distributions with the corresponding empirical distribution from the experimental dataset. Random numbers were generated using the function *runif* from the *stats* library.

For the spatial analysis, each time a new centriole appeared, the 3D pairwise distances between centrioles was calculated and labelled according to appearance relative to prior centrosomes in the droplet. This allowed keeping track of event order and, if any spatial effect of existing centrosomes on the appearance of a new centrosome was present, we would be able to detect a difference in their pairwise distances. To test this, the function *kruskal.test* of the *stats* library was used to perform the Kruskal-Wallis rank sum test on the pair-wise distances and labels. To complement this analysis, we decided to compare the distributions of pairwise distances with those expected by a spatially null model whereby centrosomes appear randomly across the available space in the droplet. To simulate this null model, sets of random points were simulated in sections of semi-spheres of similar geometry as each of the experimental droplets,

characterised by height h and diameter d. To this effect, a height z was generated which satisfied $q_1 = \frac{z\,(d^2(6h-3z)+4hz(3hz(2z))}{3d^2h^2+4h^4}$ – where q_1 was a random number between 0 and 1 – by applying the *optim* function from the *stats* library with the "Brent" method, starting with $z = 0$. This ensured that the z coordinate was selected proportionally to the area of the circle it specifies. The two extremes, $z = 0$ and $z = 1$, correspond to the lowest and highest point of the droplet, respectively. Subsequently, the coordinates x and y were generated, within the respective circle at height z, by generating a random angle θ between 0 and 2π, and a random number q_2 between 0 and 1, resulting in $x = r\cos(\theta)$ and $y = r\sin(\theta)$, where $r = a\sqrt{q_2}$, $a = 2\sqrt{(h-z)(2R-(h-z))}$ and $R = \frac{d^2+4h^2}{8h}$. The pairwise distances between simulated points were calculated in the same way as for the experimental data, and the respective empirical cumulative distributions were computed and compared to the experimental empirical distribution, as described above.

For the temporal analysis, the waiting times between centrosome births were calculated from the data and labelled according to which centrosome had just formed. Accounting for a possible change of centrosome birth rate as a function of the number of existing centrosomes, centrosome birth rates were estimated from each of the observed distributions of waiting times by Maximum Likelihood using the *fitdistr* function from the *MASS* library. The experimental data was then compared with a temporal null model whereby centrosomes form at a constant rate in time, irrespective of the existence of other centrosomes and of the volume of the droplet. To this effect, random samples of Poisson distributed waiting times were generated using the *rexp* function of the *stats* library, using the rate estimated from the waiting times between the appearance of the first and second centrosomes. The empirical cumulative distributions of these waiting times were compared to those from experimental data, as described above.

The trans-autophosphorylation of Plk4 was modelled following Lopes et al., 2015. Briefly, it is assumed that Plk4 protein is produced with constant source rate s in basal activity form B. The phosphorylation of this B form in the T-loop results in a form A_1 with higher catalytic activity. The phosphorylation of the A_1 form the degron converts it to a A_2 that is targeted for proteasome increasing its degradation rate but that keeps the same catalytic activity. The phosphorylation at the T-loop is catalysed by either low activity B form or the high activities A_1 and A_2 forms, while only the later are assumed to phosphorylate the degron of other Pkl4 forms. Both phophorylation reactions can be reverse by the constant activity of a phosphatase. We neglected the first order phosphorylation term in Lopes et al. (2015)

831 The dynamics of the three Plk4 forms is described by the following set of differential
832 equations:

833 $$\frac{dB}{dt} = s - d_0 B - aBA - bB^2 + pA_1$$

834 $$\frac{dA_1}{dt} = aBA + bB^2 - cAA_1 + pA_2 - pA_1 - d_1 A_1$$

835 $$\frac{dA_2}{dt} = cAA_1 - pA_2 - pA_2 - d_2 A_2$$

836 with $A = A_1 + A_2$.

837 The rate of *de novo* centriole formation in the explant is assumed to be proportional
838 Plk4 activity ($aA + bB$) and therefore the probability that a droplet has no centrioles F
839 decreases in time according to:

840 $$\frac{dF}{dt} = -f(aA + bB)F.$$

841 The system of four differential equations was solved numerically using the function
842 *ode* of the package *deSolve* in the software R.

843 The stochastic solutions for the same set of reactions were obtained by the Gillespie
844 algorithm as implemented in the function *ssa* of the package *GillespieSSA* in R. Each
845 simulation corresponded to a droplet where the Plk4 trans-autophosphorylation was
846 simulated independently. The biosynthesis of the first centriole was simulated as a single
847 reaction event that removes a single “precursor” F with a propensity $f(aA + bB)F$. The
848 simulated explant is assumed to form one centriole upon this event.

849 The model in differential equation and stochastic versions was used to reproduce the
850 temporal evolution of the number of explants containing at least under different
851 concentrations of Plk4. Experimentally four activity levels of Plk4 were obtained by
852 mixing the cytoplasm of eggs overexpressing Plk4 and wildtype, in different proportions
853 with expected activities relative to the overexpressing egg of 1.0, 0.5, 0.33, and 0.12
854 (Fig. 5B and Suppl. figure 6). The corresponding levels of Plk4 activity were defined in
855 the model through the source parameter $s = K, K/2, K/3, K/6$. The value of *K* and the
856 remaining parameters were adjusted by solving the ordinary differential equations for
857 variable *F* and visually comparing *(1-F)* with the experimental time course of the
858 frequencies of explants with at least one centriole (Suppl. figure 6). The adjusted
859 parameters were then used to simulate the stochastic kinetics. The parameter values of

the solutions illustrated in Supplemental figure 6 were: $K = 0.01Nmin^{-1}$, $a = 1.0/Nmin^{-1}$, $b = 0.01/Nmin^{-1}$, $c = 1.0/Nmin^{-1}$, $p = 0.45min^{-1}$, $d_0 = d_1 = 0.01min^{-1}$, $d_2 = 0.38min^{-1}$, $f = 0.34$. The value of *N* was set to 2000 molecules for the Gillespie simulations and to the unit in the ordinary differential equations.

3D-Structured Illumination Microscopy

Cytoplasmic droplets were imaged with a Plan Apo 60x NA 1.42 oil objective on a GE HealthCare Deltavision OMX system, equipped with two PCO Edge 5.5 sCMOS cameras and 488 nm and 568 nm laserlines. Spherical aberrations were minimised by matching the refractive index of the immersion oil to that of the cytosol, providing the most symmetrical point spread function. 15 seconds, multi-stack time-lapses were acquired, with 0.125 µm Z-steps and 15 frames (three angles and five phases per angle) per Z-section. Images were reconstructed in Applied Precision's softWorx software and processed using Fiji (NIH, (Schindelin et al., 2012)). Selected stills were assembled into final figures with Photoshop CS6 (Adobe).

Biochemistry

mNeonGreen purification

The mNeonGreen coding sequence was cloned with an N-terminus Streptavidin-Binding Peptide (SBP)-Tag and a flexible linker, into the pETMz expression vector (gift from the EMBL Protein Expression & Purification Facility, Heidelberg, Germany), between NcoI and BamHI restriction sites. The 6xHis-Z-tag-TEV-SBP-linker-mNeonGreen protein was expressed in BL21 (Rosetta) Competent *E. coli* at 25ºC for 5 hours. The grown liquid culture was harvested and centrifuged at 4000 rpm for 25 minutes, at 4ºC. The pellet was ressuspended in ice-cold lysis buffer containing 50 mM K-Hepes (pH 7.5), 250 mM KCl, 1mM $MgCl_2$, 1 mM DTT, 7 mM of Imidazole, 1x DNaseI and 1x Protease inhibitors. The sample was applied to a pre-chilled French-press, equilibrated with Lysis buffer, and run twice at a constant pressure (around 12kPa). The cell lysate was collected in a flask on ice and ultracentrifuged at 4°C for 25 min at 50000 rpm using a Ti-70 rotor (Beckman). The protein purification was done through affinity chromatography on a Ni-column (HiTrap chelating HP column 1 ml, GE HealthCare). The column was loaded with a filtered solution of 100 mM nickel chloride, washed extensively with milliQ water and equilibrated with wash buffer (50 mM K-Hepes (pH 7.5), 250 mM KCl, 1mM $MgCl_2$, 1 mM DTT, 7 mM of Imidazole). The clarified lysate was

applied to the column (at 1.5 ml/min), followed by 200 ml wash buffer. The protein was eluted at 1.5 ml/min with elution buffer: 50 mM K-Hepes (pH 7.5), 250 mM KCl, 1mM $MgCl_2$, 1 mM DTT, 400 mM of Imidazole. 1 ml sample fractions were collected and kept at 4ºC. The most concentrated samples were pooled together and their N-terminus 6xHis-Z-tag was cleaved with TEV protease overnight at 4ºC by treating with 150U TEV/mg of protein. The following day, the cleaved protein was passed through a column for size-exclusion chromatography to remove contaminants, the cleaved tag and the TEV protease (with Tiago Bandeiras at IBET, Oeiras, Portugal). Additionally, the elution buffer was exchanged to a storage buffer: 50 mM K-Hepes (pH 7.8), 100 mM KCl, 2 mM $MgCl_2$, 1 mM DTT, 1 mM EGTA. The HiLoad Superdex 75 16/60 (GE HealthCare) gel filtration column was equilibrated with storage buffer for 1hour. The sample was spun at 15000 rpm for 15 min at 4ºC and the clear fraction was applied to the gel filtration column coupled to an AKTA device at 1 ml/min. The cleaved mNeonGreen protein was concentrated approximately 5 times using Amicon 10K Centrifugal filters. Pure glycerol was added at 5% v/v and small aliquots were snap-frozen in liquid nitrogen and stored at -80ºC.

Plk4 titration in cytoplasmic extract

Plk4 dilution was accomplished by mixing cytoplasm from flies with different genetic composition. Unfertilised eggs collected from females overexpressing Plk4 in the germline (genotype: V32-Gal4/ pUb-Spd2–GFP; Jupiter-mCherry/pUASp-GFP–Plk4) were homogenised in unfertilised eggs from females without the transgenic pUASp element (genotype: V32-Gal4/ pUb-Spd2–GFP; Jupiter–mCherry), where all components are at wild-type levels, specifically diluting overall Plk4 concentration in the cytoplasm. Different final Plk4 concentrations were achieved by mixing Plk4 overexpression:wildtype eggs at the following ratios: 6:0 (“1” relative Plk4 concentration, control); 3:3 (“0.5” relative Plk4 concentration); 2:4 (“0.33” relative Plk4 concentration) and 1:5 (“0.16” relative Plk4 concentration). Small droplets were produced from the cytoplasmic mixtures and images were acquired for 40 minutes. All time-lapse acquisitions within this section were performed at 1 minute time-interval with 0.45 µm optical sections, using a Plan Apo VC 60x 1.2 NA water objective.

Fluorescence Correlation Spectroscopy (FCS) data acquisition and analysis

Standard rhodamine 6G calibration

All FCS measurements were performed on a point-scanning confocal microscope (Zeiss LSM780 Confocor3) equipped with a UV-VIS-IR C Achromat 40X 1.2 NA water-immersion objective and a gallium arsenide detector array wavelength selected between 491-561nm. Before each experiment the system was aligned using a high concentration and calibrated using a low concentration Rhodamin 6G solution in water. The known diffusion coefficient of rhodamine 6G (410 $\mu m^2/s$) (Majer and Zick, 2015) allowed us to determine the lateral beam waist (w_{xy} = 232 nm) and the structure factor (S = 5.77) of the focused laser (Point Spread Function, PSF). The resultant volume of illumination is calculated through:

$$Veff = pi^{(3/2)} \cdot w_{xy}^2 \cdot w_z = pi^{(3/2)} \cdot w_{xy}^2 \cdot S \cdot w_{xy} = 0.401\ um^3 = 4.01 \cdot 10^{-16}\ l$$

The values for w_{xy} and S were used as constants in the subsequent model-based fittings of the autocorrelation functions (ACF) and the volume was used to calculate the concentration (see below).

Calibration with purified mNeonGreen

mNeonGreen fluorescent tag was first measured in a cytoplasm-compatible buffer. Fluorescence intensity in time (I(t)) was recorded as 6 iterations of 10s. Each 10s trace was autocorrelated into an ACF, G(τ), using the Zeiss onboard autocorrelator which calculates the self-similarity through:

$$G(\tau)=\langle dI(t) \cdot dI(t+\tau)\rangle \cdot \langle I(t)\rangle^{-2}$$

Here <> denotes the time-average, $dI(t)=I(t)-\langle I(t)\rangle$ and τ is called the timelag. The resulting G(τ) curves of the fluorophores in buffer were readily fitted using a regular 3D diffusion model:

$$G(\tau)=1/N \cdot GT(\tau) \cdot GD(\tau)$$

where N reflects the number of moving particles in the confocal volume and GT(τ) is the correlation function associated to blinking/triplet kinetics:

$$GT(\tau) = 1 + T \cdot (1 - T)^{-1} \cdot \exp^{(\tau/\tau t)}$$

Where T is the fraction of molecules in the dark state and τt the lifetime of the darkstate. GD(τ) is the correlation function associated to diffusion which in this case is simple Brownian diffusion in 3D:

$$GD(\tau) = (1 + \tau/\tau_D)^{-1} \cdot (1 + S^{-2} \cdot \tau / \tau_D)^{-(1/2)}$$

These fittings allowed us to measure the number of molecules in the confocal volume and therefore their brightness (<I(t)> / N) together with the characteristic diffusion times (τ_D).

The above model fit is based on the assumption that there are only two characteristic timescales generating the ACF. In order to get a model free estimate of the number of timescales involved we used a Maximum Entropy Method based fitting (MEMfit) of the combined and normalised ACFs of each experiment. MEMfit analyses the FCS autocorrelation data in terms of a quasicontinuous distribution of diffusing components making it an ideal model to examine the ACF of a highly heterogeneous system without prior knowledge of the amount of diffusing species.

To be able to quantify the brightness of individual fluorescent tags in an embryo the purified mNeonGreen was injected into pUb-RFP-**β**2-Tubulin dechorionated embryos. An anomalous coefficient had to be included to fit the resultant ACF:

$$GD(\tau) = (1 + (\tau/\tau_D)^a)^{-1} \cdot (1 + S^{-2} \cdot (\tau / \tau_D)^a)^{-(1/2)}$$

For simple Brownian diffusion a = 1 and the fit function is identical to the one used to fit the fluorophores in buffer. However, for fluorophores injected into the cytosol of embryos the fitting algorithm gave an anomalous coefficient of a = 0.8. An anomalous coefficient smaller than 1 indicates constrained diffusion and could be caused by the more crowded environment in the yolk. In addition, the large amount of (uncorrelated) autofluorescence generated by the yolk leads to an underestimation of the brightness therefore requiring a background correction factor. The background values were determined per excitation power from embryos lacking the Plk4 reporter. If the background itself does not autocorrelate it has no influence on the obtained timescales in the data. Nevertheless, the background will impact the absolute number, N, and consequently also the calculated brightness. Therefor, all the measurements were background corrected during via:

$$Ncorr = N \cdot ((<I(t)> - BG) / <I(t)>)^2$$

Where BG is the measured background from embryos lacking the reporter fluorophore. Consequently the corrected brightness was calculated as:

$$BNcorr = (<I(t)> - BG) / Ncorr$$

Finally, any 1 millisecond-binned intensity trace that contained changes in average intensity (most likely arising from yolk spheres moving through the confocal spot during the measurement) were discarded from further analysis.

mNeonGreen-Plk4 measurements in embryos

For the measurements of mNeonGreen-Plk4, embryo staging was done based on the pUb-RFP-**β**2-Tubulin reporter. We chose embryos at blastoderm stage, in division cycles 10 or 11. Before each FCS acquisition series, a large field-of-view image of the embryo was acquired. Six different, 10 seconds long intensity traces were measured at the inter-nuclear cytoplasmic space of the syncytium. The 10s measurement was long enough to obtain sufficient passage events and short enough to avoid each trace to be contaminated by events that do not arise from mNeonGreen-Plk4 diffusing in the cytosol.

From these measurements, the MEMfit method on the normalised ACF indicates three timescales for the tagged-Plk4 molecules. A first timescale of 5-50 µs corresponding to the triplet state dynamics that were similarly found in both the buffer as well as from fluorophores injected in the embryo. A second timescale of about 0.8ms, most likely coming from the diffusion of a Plk4 monomer (see similarity to mNeonGreen monomer in cytosol). And a third timescale of diffusion that is much slower, 9ms. In order to fit the ACFs the diffusional part of the fit function was associated with two components:

$$GD(\tau) = f \cdot GD1(\tau) + (1 - f) \cdot GD2(\tau) =$$

$$f \cdot [(1 + \tau/\tau_{D1})^{-1} \cdot (1 + S^{-2} \cdot \tau / \tau_{D1})^{-(1/2)}] + (1 - f) \cdot [(1 + \tau/\tau_{D2})^{-1} \cdot (1 + S^{-2} \cdot \tau / \tau_{D2})^{-(1/2)}]$$

The fraction f corresponds to the fast diffusing Plk4. The Diffusion Coefficient of each of the components can be calculated from the diffusion timescales τD via:

$$D = w_{xy}^2 / 4 \cdot \tau_D$$

In vitro experiments

Drosophila melanogaster cell culture

Drosophila (DMEL) cells were cultured in Express5 SFM (GIBCO, USA) supplemented with 1x L-Glutamine-Penicillin-Streptomycin. Double-stranded RNA (dsRNA) synthesis was performed as previously described (Bettencourt-Dias et al., 2004). 2 million cells were plated and treated for 12 days with 40 µg dsRNA against Plk4

or mCherry (control), replacing the dsRNA every 4 days. Cells were fixed at day 10 to confirm centriole depletion and treatment with dsRNA agains PCM was initiated. Cells were then treated for 6 days with different amounts and combinations of dsRNA: 80 µg mCherry alone, 20 µg of individual PCM components – Cnn, Asl, D-Plp, Spd2 or **γ**-tubulin 23C – or combinations of two – Cnn + Spd2 or Cnn + D-Plp – or four components – Cnn + Asl + D-Plp + Spd2 (referred to as 'All PCM'). Primers used for dsRNA synthesis are listed in Suppl. Table S5.

Immunostaning and imaging of *D. melanogaster* cultured cells

DMEL cells were plated onto clean glass coverslips and allowed to adhere for 1 hour and 30 min. The media was removed and cells were fixed at -20ºC for 10 min in chilled methanol. Cells were permeabilised and washed in D-PBSTB (1x Dulbecco's Phosphate Buffered Saline pH 7.3, with 0.1% Triton X-100 and 1% BSA) for 1 hour. Cells were incubated overnight at 4ºC with primary antibodies – rat anti-Sas4 (dilution 1:500) kindly provided by David Glover (University of Cambridge, UK) and rabbit anti-CP110 (dilution 1:10000; Metabion) – diluted in D-PBSTB. Cells were washed in D-PBSTB and incubated for 1hour 30 min at room temperature with secondary antibodies – donkey anti-rat Alexa 555 (dilution 1:1000; Molecular Probes) and donkey anti-rabbit Alexa 647 (dilution 1:1000; Jackson Immunoresearch Laboratories) – and DAPI (dilution 1:200) in D-PBSTB. Cells were washed and mounted with Dako Faramount Aqueous Mounting Medium (S3025, Agilent).

Cell imaging was conducted on a Nikon Eclipse Ti-E microscope equipped with a Yokogawa CSU-X1 Spinning Disk confocal scanner. Images were recorded with a EMCCD Photometrics 512 camera. Optical sections of 0.3 µm thickness were acquired with a Plan Apo 100x 1.49 NA oil immersion objective using a piezoelectric stage (737.2SL, Physik Instrumente), controlled by Metamorph 7.5 software. Centriole number was scored in 300 cells per treatment, per independent experiment. Data is presented as average (with standard error mean, S.E.M.) of two independent experiments. We tested all counts with a Chi-square test against the null-hypothesis that the outcome is random. Then, each 16d test condition was compared to the 16d mCherry control condition with a 2-proportions Z-test and H0 that the proportions of cells with centrioles are equal versus HA that the proportion in the test is smaller. The significance level for multiple testing was Bonferroni corrected. Significance level was $p = 0.01$. All images were processed with ImageJ (NIH, USA) and Adobe Photoshop CS6 (Adobe Systems, USA), and the final figures were assembled in Adobe Illustrator CS6 (Adobe Systems, USA).

1052

Acknowledgments

We would like to thank the Central Imaging and Flow Cytometry Facility (CIFF) at the National Centre for Biological Sciences (NCBS) in Bangalore, where all FCS experiments were performed.

We acknowledge the technical support of IGC's Advanced Imaging Facility (AIF), in particular Gabriel Martins and Nuno Pimpão Martins. IGC's AIF is supported by the national Portuguese funding ref# PPBI-POCI-01-0145-FEDER-022122, co-financed by Lisboa Regional Operational Programme (Lisboa 2020), under the Portugal 2020 Partnership Agreement, through the European Regional Development Fund (FEDER) and Fundação para a Ciência e a Tecnologia (FCT, Portugal).

We thank IGC's Fly Facility and Fly Transgenesis Facility supported by Congento (LISBOA-01-0145-FEDER-022170), co-financed by Lisboa Regional Operational Program (Lisboa 2020) under the Portugal 2020 Partnership Agreement through the European Regional Development Fund (FEDER) and Fundação para a Ciência e a Tecnologia (FCT, Portugal). Transgenic fly stocks were obtained from Bloomington Drosophila Stock Center (NIH742 P40OD018537).

We acknowledge financial support from Boehringer Ingelheim Fonds PhD Fellowship awarded to C. Nabais, Human Frontiers Science Program (HFSP) Young Investigator Grant (RGY0083/2016) awarded to I.A. Telley supporting J. de–Carvalho, the Fundação para Ciência e a Tecnologia (FCT) supporting I.A. Telley (Investigador FCT IF/00082/2013), the EU FP7-PEOPLE-2013-CIG (Nº 818743) awarded to I.A. Telley, ERC-2010-StG-261344-CentriolStructure&Number and an ERC-2015-CoG-683258-Birth&Death awarded to M. Bettencourt-Dias, and the Gulbenkian Foundation (FCG). T.S. van Zanten acknowledges an EMBO fellowship (ALTF 1519-2013) and a NCBS Campus fellowship. S. Mayor acknowledges a JC Bose Fellowship from DST (Government of India), support from the NCBS-Max Planck Lipid Centre, a grant from HFSP RGP0027/2012, and support from Wellcome Trust/DBT India Alliance Margdarshi Fellowship (IA/M/15/1/502018).

We thank Tiago Bandeiras at Instituto de Biologia Experimental e Tecnológica (IBET), Oeiras, for the gel filtration chromatography conducted in his facility with Micael Freitas.

We thank Tomer Avidor-Reiss, Daniel St Johnston, Yoshihiro Inoue and Jordan Raff for sharing transgenic fly lines. We thank David Glover, Jordan Raff and Tim Megraw for providing antibodies.

We thank members of the Cell Cycle Regulation lab at IGC for giving feedback to earlier versions of the manuscript.

Author contributions

Conceptualization: CN, IAT, MBD

Methodology: CN, JdC, IAT (egg explant assay); CN, TvZ (FCS measurements)

Software: DP, JC (design and implementation of model simulations)

Validation: CN, JdC, DP, TvZ, SM, JC, IAT, MBD

Investigation: CN, JdC (performing data collection egg explants); CN, TvZ (performing data collection in FCS measurements); DP, JC (collecting in silico data)

Analysis: CN, IAT (experimental data from egg explants, eggs and cell culture); TvZ, SM (FCS data); DP, JC (theoretical model)

Resources: CN (CRISPR fly line, vectors and plasmid design, recombinant protein purification); PD (genotyping); IAT (design of micromanipulation microscope)

Visualization of data: CN, DP, TvZ, IAT

Writing – original draft: CN

Writing – review and editing: CN, SM, JC, IAT, MBD

Supervision and coordination: IAT, MBD

Competing interests

The authors declare no competing interests for this study.

References

Al Jord, A., A.I. Lemaître, N. Delgehyr, M. Faucourt, N. Spassky, and A. Meunier. 2014. Centriole amplification by mother and daughter centrioles differs in multiciliated cells. Nature. 516:104–107. doi:10.1038/nature13770.

Aldrich, H.C. 1967. The Ultrastructure of Meiosis in Three Species of Physarum. Mycologia. 59:127–148. doi:10.2307/3756947.

Aydogan, M.G., T.L. Steinacker, M. Mofatteh, L. Gartenmann, A. Wainman, S. Saurya, P.T. Conduit, F.Y. Zhou, M.A. Boemo, and J.W. Raff. 2019. A free-running oscillator times and executes centriole biogenesis. BioRxiv.

Banterle, N., and P. Gönczy. 2017. Centriole Biogenesis: From Identifying the Characters to Understanding the Plot. Annu. Rev. Cell Dev Biol. 33:23–49. doi: 10.1146/annurev-cellbio-100616-060454.

Bauer, M., F. Cubizolles, A. Schmidt, and E.A. Nigg. 2016. Quantitative analysis of human centrosome architecture by targeted proteomics and fluorescence imaging. EMBO J. 35:2152–2166. doi:10.15252/embj.

Bettencourt-Dias, M., A. Rodrigues-Martins, L. Carpenter, M. Riparbelli, L. Lehmann, M.K. Gatt, N. Carmo, F. Balloux, G. Callaini, and D.M. Glover. 2005. SAK/PLK4 is required for centriole duplication and flagella development. Curr. Biol. 15:2199–2207. doi:10.1016/j.cub.2005.11.042.

Bettencourt-Dias, M., F. Hildebrandt, D. Pellman, G. Woods, and S.A. Godinho. 2011. Centrosomes and cilia in human disease. Trends Genet. 27:307–15. doi:10.1016/j.tig.2011.05.004.

Bettencourt-Dias, M., R. Giet, R. Sinka, A. Mazumdar, W.G. Lock, F. Balloux, P.J. Zafiropoulos, S. Yamaguchi, S. Winter, R.W. Carthew, M. Cooper, D. Jones, L. Frenz, and D.M. Glover. 2004. Genome-wide survey of protein kinases required for cell cycle progression. Nature. 432:980–987. doi.org/10.1038/nature03160.

Blachon, S., J. Gopalakrishnan, Y. Omori, A. Polyanovsky, A. Church, D. Nicastro, J. Malicki, and T. Avidor-Reiss. 2008. Drosophila asterless and vertebrate Cep152 Are orthologs essential for centriole duplication. Genetics. 180:2081–94. doi:10.1534/genetics.108.095141.

Boese, C.J., J. Nye, D.W. Buster, T.A. Mclamarrah, A.E. Byrnes, K.C. Slep, N.M. Rusan, and G.C. Rogers. 2018. Asterless is a Polo-like kinase 4 substrate that both activates and inhibits kinase activity depending on its phosphorylation state. Mol. Biol. Cell. 29:2874–2886. doi: 10.1091/mbc.

Breslow, D.K., and A.J. Holland. 2019. Mechanism and Regulation of Centriole and Cilium Biogenesis. Annu. Rev. Biochem. 88:11.1-11.34. doi: 10.1146/annurev-biochem-013118-111153.

1144 Breugel, M. Van, M. Hirono, A. Andreeva, H. Yanagisawa, S. Yamaguchi, Y. Nakazawa, N.
1145 Morgner, M. Petrovich, C. V Robinson, C.M. Johnson, D. Veprintsev, and H. Road. 2011.
1146 Structures of Sas-6 Suggest Its Organization in Centrioles. Science. 331:1196–1199. doi:
1147 10.1126/science.1199325.

1148 Chang, C., W. Hsu, J. Tsai, C.C. Tang, and T.K. Tang. 2016. CEP295 interacts with microtubules
1149 and is required for centriole elongation. J. Cell Sci. 129:2501–2513. doi: 10.1242/jcs.186338.

1150 Charvin, G., C. Oikonomou, E.D. Siggia, and F.R. Cross. 2009. Origin of Irreversibility of Cell
1151 Cycle Start in Budding Yeast. PLoS Biol. 8. doi:10.1371/journal.pbio.1000284.

1152 Conduit, P.T., A. Wainman, Z.A. Novak, T.T. Weil, and J.W. Raff. 2015. Re-examining the role of
1153 Drosophila Sas-4 in centrosome assembly using two-colour-3D-SIM FRAP. Elife. 4.
1154 doi:10.7554/eLife.08483.

1155 Cunha-Ferreira, I., A. Rodrigues-Martins, I. Bento, M. Riparbelli, W. Zhang, E. Laue, G. Callaini,
1156 D.M. Glover, and M. Bettencourt-Dias. 2009. The SCF/Slimb ubiquitin ligase limits centrosome
1157 amplification through degradation of SAK/PLK4. Curr. Biol. 19:43–49.
1158 doi:10.1016/j.cub.2008.11.037.

1159 Cunha-Ferreira, I., I. Bento, A. Pimenta-Marques, S.C. Jana, M. Lince-Faria, P. Duarte, J.
1160 Borrego-Pinto, S. Gilberto, T. Amado, D. Brito, A. Rodrigues-Martins, J. Debski, N. Dzhindzhev,
1161 and M. Bettencourt-Dias. 2013. Regulation of Autophosphorylation Controls PLK4 Self-
1162 Destruction and Centriole Number. Curr. Biol. 23:2245–54. doi:10.1016/j.cub.2013.09.037.

1163 Dammermann, A., T. Müller-Reichert, L. Pelletier, B. Habermann, A. Desai, and K. Oegema.
1164 2004. Centriole assembly requires both centriolar and pericentriolar material proteins. Dev. Cell.
1165 7:815–829. doi:10.1016/j.devcel.2004.10.015.

1166 de-Carvalho, J., O. Deshpande, C. Nabais, and I.A. Telley. 2018. A cell-free system of Drosophila
1167 egg explants supporting native mitotic cycles. 144. 1st ed. Elsevier Inc. 233–257 pp. doi:
1168 10.1016/bs.mcb.2018.03.011.

1169 Delattre, M., C. Canard, and P. Gönczy. 2006. Sequential protein recruitment in C. elegans
1170 centriole formation. Curr. Biol. 16:1844–9. doi:10.1016/j.cub.2006.07.059.

1171 Deneke, V.E., A. Puliafito, D. Krueger, A. V Narla, A. De Simone, L. Primo, M. Vergassola, S. De
1172 Renzis, and S. Di Talia. 2019. Self-Organized Nuclear Positioning Synchronizes the Cell Cycle in
1173 Drosophila Embryos. Cell. 177:925–941. doi:10.1016/j.cell.2019.03.007.

1174 Dingle, A.D., and C. Fulton. 1966. Development of the flagellar apparatus of Naegleria. J. Cell
1175 Biol. 31:43–54. doi: 10.1083/jcb.31.1.43.

1176 Dirksen, E.R. 1961. The presence of centrioles in artificially activated sea urchin eggs. J. Cell
1177 Biol. 11:244–247. doi: 10.1083/jcb.11.1.244.

1178 Ferree, P.M., K. McDonald, B. Fasulo, and W. Sullivan. 2006. The origin of centrosomes in
1179 parthenogenetic hymenopteran insects. Curr. Biol. 16:801–7. doi:10.1016/j.cub.2006.03.066.

1180 Fritz-Laylin, L.K., Y.Y. Levy, E. Levitan, S. Chen, W.Z. Cande, E.Y. Lai, and C. Fulton. 2016.
1181 Rapid centriole assembly in Naegleria reveals conserved roles for both de novo and mentored
1182 assembly. Cytoskeleton. 73:109–116. doi:10.1002/cm.21284.

1183 Fu, J., Z. Lipinszki, H. Rangone, M. Min, C. Mykura, J. Chao-chu, S. Schneider, N.S. Dzhindzhev,
1184 M. Gottardo, G. Riparbelli, G. Callaini, and D.M. Glover. 2016. Conserved Molecular Interactions
1185 in Centriole-to-Centrosome Conversion. Nat. Cell Biol. 18:87–99. doi:10.1038/ncb3274.

1186 Fulton, C., and A.D. Dingle. 1971. Basal bodies, but not centrioles, in Naegleria. J. Cell Biol.
1187 51:826–835. doi:10.1083/jcb.51.3.826.

1188 Godfrey, M., S.A. Touati, M. Kataria, A. Jones, A.P. Snijders, and F. Uhlmann. 2017. PP2ACdc55
1189 Phosphatase Imposes Ordered Cell-Cycle Phosphorylation by Opposing Threonine
1190 Phosphorylation. Mol. Cell. 65:393–402. doi:10.1016/j.molcel.2016.12.018.

1191 Godinho, S.A., and D. Pellman. 2014. Causes and consequences of centrosome abnormalities
1192 in cancer. Philos. Trans. R. Soc. B Biol. Sci. 369. doi:10.1098/rstb.2013.0467.

1193 Godinho, S.A., R. Picone, M. Burute, R. Dagher, Y. Su, C.T. Leung, K. Polyak, J.S. Brugge, M.
1194 Thery, and D. Pellman. 2014. Oncogene-like induction of cellular invasion from centrosome
1195 amplification. Nature. 510:167–171. doi:10.1038/nature13277.

1196 Grimes, G.W. 1973a. Origin and development of kinetosomes in Oxytricha fallax. J. Cell Sci.
1197 13:43–53.

1198 Grimes, G.W. 1973b. Morphological discontinuity of kinetosomes during the life cycle of Oxytricha
1199 fallax. J. Cell Biol. 57:229–232. doi: 10.1083/jcb.57.1.229.

1200 Guderian, G., J. Westendorf, A. Uldschmid, and E. A. Nigg. 2010. Plk4 trans-autophosphorylation
1201 regulates centriole number by controlling betaTrCP-mediated degradation. J. Cell Sci. 123:2163–
1202 2169. doi:10.1242/jcs.068502.

1203 Guichard, P., V. Hamel, M. Le Guennec, N. Banterle, I. Iacovache, V. Nemcıkova, I. Fluckiger,
1204 K.N. Goldie, H. Stahlberg, D. Levy, B. Zuber, and P. Gonczy. 2017. Cell-free reconstitution
1205 reveals centriole cartwheel assembly mechanisms. Nat. Commun. 8. doi:10.1038/ncomms14813.

1206 Gutierrez-Escribano, P., and P. Nurse. 2015. A single cyclin–CDK complex is sufficient for both
1207 mitotic and meiotic progression in fission yeast. Nat. Commun. 6. doi:10.1038/ncomms7871.

1208 Habedanck, R., Y.D. Stierhof, C.J. Wilkinson, and E.A. Nigg. 2005. The Polo kinase PLK4
1209 functions in centriole duplication. Nat. Cell Biol. 7:1140–1146. doi: 10.1038/ncb1320.

1210 Harvey, E.B. 1936. Parthenogenetic Merogony or Cleavage without Nuclei in Arbacia punctulata.
1211 Mar. Biol. Lab. 71:101–121. doi: 10.2307/1537411.

1212 Holland, A.J., D. Fachinetti, Q. Zhu, M. Bauer, I.M. Verma, E. A. Nigg, and D.W. Cleveland. 2012.
1213 The autoregulated instability of Polo-like kinase 4 limits centrosome duplication to once per cell
1214 cycle. Genes Dev. 26:2684–2689. doi:10.1101/gad.207027.112.

1215 Horner, V.L., A. Czank, J.K. Jang, N. Singh, B.C. Williams, J. Puro, E. Kubli, S.D. Hanes, K.S.
1216 McKim, M.F. Wolfner, and M.L. Goldberg. 2006. The Drosophila Calcipressin Sarah Is Required
1217 for Several Aspects of Egg Activation. Curr. Biol. 16:1441–1446. doi:10.1016/j.cub.2006.06.024.

1218 Idei, M., K. Osada, S. Sato, T. Nakayama, T. Nagumo, and D.G. Mann. 2013. Sperm
1219 ultrastructure in the diatoms Melosira and Thalassiosira and the significance of the 9 + 0
1220 configuration. Protoplasma. 250:833–850. doi:10.1007/s00709-012-0465-8.

1221 Ito, D., S. Zitouni, S.C. Jana, P. Duarte, J. Surkont, Z. Carvalho-Santos, J.B. Pereira-Leal, M.G.
1222 Ferreira, and M. Bettencourt-Dias. 2019. Pericentrin-mediated SAS-6 recruitment promotes
1223 centriole assembly. Elife. 8. doi: 10.7554/eLife.41418.

1224 Izquierdo, D., W.J. Wang, K. Uryu, and M.F.B. Tsou. 2014. Stabilization of cartwheel-less
1225 centrioles for duplication requires CEP295-mediated centriole to centrosome conversion. Cell.
1226 Rep. 8:957–965. doi:10.1016/j.celrep.2014.07.022.

1227 Jaqaman, K., D. Loerke, M. Mettlen, H. Kuwata, S. Grinstein, S.L. Schmid, and G. Danuser. 2008.
1228 Robust single-particle tracking in live-cell time-lapse sequences. Nat. Methods. 5:695–702.
1229 doi:10.1038/nmeth.1237.

1230 Joukov, V., and A. De Nicolo. 2019. The Centrosome and the Primary Cilium: The Yin and Yang
1231 of a Hybrid Organelle. Cells. 8. doi: 10.3390/cells8070701.

1232 Keller, D., M. Orpinell, N. Olivier, M. Wachsmuth, R. Mahen, R. Wyss, V. Hachet, J. Ellenberg, S.
1233 Manley, and P. Gönczy. 2014. Mechanisms of HsSAS-6 assembly promoting centriole formation
1234 in human cells. J. Cell Biol. 204:697–712. doi:10.1083/jcb.201307049.

1235 Kemp, C.A., K.R. Kopish, P. Zipperlen, J. Ahringer, and K.F.O. Connell. 2004. Centrosome
1236 Maturation and Duplication in C. elegans Require the Coiled-Coil Protein SPD-2. Dev. Cell.
1237 6:511–523. doi: 10.1016/s1534-5807(04)00066-8.

1238 Khodjakov, A., C.L. Rieder, G. Sluder, G. Cassels, O. Sibon, and C. Wang. 2002. De novo
1239 formation of centrosomes in vertebrate cells arrested during S phase. J. Cell Biol. 158:1171–
1240 1181. doi:10.1083/jcb.200205102.

1241 Kitagawa, D., I. Vakonakis, N. Olieric, M. Hilbert, D. Keller, V. Olieric, M. Bortfeld, M.C. Erat, I.
1242 Flückiger, P. Gönczy, and M.O. Steinmetz. 2011. Structural basis of the 9-fold symmetry of
1243 centrioles. Cell. 144:364–375. doi:10.1016/j.cell.2011.01.008.

1244 Kitazawa, D., T. Matsuo, K. Kaizuka, C. Miyauchi, D. Hayashi, and Y.H. Inoue. 2014. Orbit/CLASP
1245 is required for myosin accumulation at the cleavage furrow in Drosophila male meiosis. PLoS
1246 One. 9. doi:10.1371/journal.pone.0093669.

1247 Klebba, J.E., B.J. Galletta, J. Nye, K.M. Plevock, D.W. Buster, N. A Hollingsworth, K.C. Slep, N.M.
1248 Rusan, and G.C. Rogers. 2015b. Two Polo-like kinase 4 binding domains in Asterless perform
1249 distinct roles in regulating kinase stability. J. Cell Biol. 208:401–414. doi:10.1083/jcb.201410105.

1250 Klebba, J.E., D.W. Buster, A.L. Nguyen, S. Swatkoski, M. Gucek, N.M. Rusan, and G.C. Rogers.
1251 2013. Polo-like Kinase 4 Autodestructs by Generating Its Slimb-Binding Phosphodegron. Curr.
1252 Biol. 23:2255–61. doi:10.1016/j.cub.2013.09.019.

1253 Klebba, J.E., D.W. Buster, T.A. McLamarrah, N.M. Rusan, and G.C. Rogers. 2015a.
1254 Autoinhibition and relief mechanism for Polo-like kinase 4. Proc. Natl. Acad. Sci. 112:E657–E666.
1255 doi:10.1073/pnas.1417967112.

1256 Kleylein-Sohn, J., J. Westendorf, M. Le Clech, R. Habedanck, Y.D. Stierhof, and E. A Nigg. 2007.
1257 Plk4-induced centriole biogenesis in human cells. Dev. Cell. 13:190–202.
1258 doi:10.1016/j.devcel.2007.07.002.

1259 Kuhn, M., A.A. Hyman, and A. Beyer. 2014. Coiled-Coil Proteins Facilitated the Functional
1260 Expansion of the Centrosome. Plos Comput. Biol. 10. doi:10.1371/journal.pcbi.1003657.

1261 La Terra, S., C.N. English, P. Hergert, B.F. McEwen, G. Sluder, and A. Khodjakov. 2005. The de
1262 novo centriole assembly pathway in HeLa cells: cell cycle progression and centriole
1263 assembly/maturation. J. Cell Biol. 168:713–722. doi:10.1083/jcb.200411126.

1264 Lambrus, B., K.M. Clutario, V. Daggubati, M. Snyder, G. Sluder, and A. Holland. 2015. p53
1265 protects against genome instability following centriole duplication failure. J. Cell Biol. 210:63–77.
1266 doi: 10.1083/jcb.201502089.

1267 Leda, M., A.J. Holland, and A.B. Goryachev. 2018. Autoamplification and Competition Drive
1268 Symmetry Breaking: Initiation of Centriole Duplication by the PLK4-STIL Network. iScience.
1269 8:222–235. doi:10.1016/j.isci.2018.10.003.

1270 Lerit, D.A., H.A. Jordan, J.S. Poulton, C.J. Fagerstrom, B.J. Galletta, M. Peifer, and N.M. Rusan.
1271 2015. Interphase centrosome organization by the PLP-Cnn scaffold is required for centrosome
1272 function. J. Cell Biol. 210:79–97. doi:10.1083/jcb.201503117.

1273 Levine, M.S., B. Bakker, B. Boeckx, J. Moyett, J. Lu, D.C. Spierings, P.M. Lansdorp, D.W.
1274 Cleveland, F. Foijer, and A.J. Holland. 2018. Centrosome amplification is sufficient to promote
1275 spontaneous tumorigenesis in mammals. Dev. Cell. 40:313–322.
1276 doi:10.1016/j.devcel.2016.12.022.

1277 Lopes, C.A.M., M. Mesquita, A.I. Cunha, J. Cardoso, S. Carapeta, C. Laranjeira, A.E. Pinto, J.B.
1278 Pereira-Leal, A. Dias-Pereira, M. Bettencourt-Dias, and P. Chaves. 2018. Centrosome
1279 amplification arises before neoplasia and increases upon p53 loss in tumorigenesis. J. Cell Biol.
1280 217:2353–2363. doi:10.1083/jcb.201711191.

1281 Lopes, C.A.M., S.C. Jana, I. Cunha-Ferreira, S. Zitouni, I. Bento, P. Duarte, S. Gilberto, F. Freixo,
1282 A. Guerrero, M. Francia, M. Lince-Faria, J. Carneiro, and M. Bettencourt-Dias. 2015. PLK4 trans-
1283 Autoactivation Controls Centriole Biogenesis in Space. Dev. Cell. 35:222–235.
1284 doi:10.1016/j.devcel.2015.09.020.

1285 Lowe, N., J.S. Rees, J. Roote, E. Ryder, I.M. Armean, G. Johnson, E. Drummond, H. Spriggs, J.
1286 Drummond, J.P. Magbanua, H. Naylor, R. Bastock, S. Huelsmann, V. Trovisco, M. Landgraf, S.
1287 Knowles-barley, J.D. Armstrong, H. White-cooper, C. Hansen, R.G. Phillips, T. Uk, D. Protein, S.
1288 Consortium, K.S. Lilley, S. Russell, and D.S. Johnston. 2014. Analysis of the expression patterns,
1289 subcellular localisations and interaction partners of Drosophila proteins using a pigP protein trap
1290 library. Development. 141:3994–4005. doi:10.1242/dev.111054.

1291 Mahen, R., A.D. Jeyasekharan, N.P. Barry, and A.R. Venkitaraman. 2011. Continuous polo-like
1292 kinase 1 activity regulates diffusion to maintain centrosome self-organization during mitosis. Proc.
1293 Natl. Acad. Sci. 108:9310–9315. doi: 10.1073/pnas.1101112108.

1294 Mahoney, N.M., G. Goshima, A.D. Douglass, and R.D. Vale. 2006. Making Microtubules and
1295 Mitotic Spindles in Cells without Functional Centrosomes. Curr. Biol. 564–569.
1296 doi:10.1016/j.cub.2006.01.053.

1297 Majer, G., and K. Zick. 2015. Accurate and absolute diffusion measurements of Rhodamine 6G
1298 in low-concentration aqueous solutions by the PGSE-WATERGATE sequence. J. Chem. Phys.
1299 142. doi: 10.1063/1.4919054.

1300 Marshall, W.F., Y. Vucica, and J.L. Rosenbaum. 2001. Kinetics and regulation of de novo centriole
1301 assembly: Implications for the mechanism of centriole duplication. Curr. Biol. 11:308–17. doi:
1302 10.1016/s0960-9822(01)00094-x.

1303 Marteil, G., A. Guerrero, A.F. Vieira, B.P. De Almeida, P. Machado, S. Mendonça, M. Mesquita,
1304 B. Villarreal, I. Fonseca, M.E. Francia, K. Dores, N.P. Martins, S.C. Jana, E.M. Tranfield, N.L.
1305 Barbosa-Morais, J. Paredes, D. Pellman, S.A. Godinho, and M. Bettencourt-Dias. 2018. Over-
1306 elongation of centrioles in cancer promotes centriole amplification and chromosome
1307 missegregation. Nat. Commun. 9. doi:10.1038/s41467-018-03641-x.

1308 Mclamarrah, T.A., D.W. Buster, B.J. Galletta, C.J. Boese, J.M. Ryniawec, N.A. Hollingsworth,
1309 A.E. Byrnes, C.W. Brownlee, K.C. Slep, N.M. Rusan, and G.C. Rogers. 2018. An ordered pattern
1310 of Ana2 phosphorylation by Plk4 is required for centriole assembly. J. Cell Biol. 217:1217–1231.
1311 doi: 10.1083/jcb.201605106.

1312 Mercey, O., A.A. Jord, P. Rostaing, A. Mahuzier, A. Fortoul, A. Boudjema, M. Faucourt, N.
1313 Spassky, and A. Meunier. 2019a. Dynamics of centriole amplification in centrosome-depleted
1314 brain multiciliated progenitors. Sci. Rep. 9. doi:10.1038/s41598-019-49416-2.

1315 Mercey, O., M.S. Levine, G.M. Lomastro, P. Rostaing, E. Brotslaw, V. Gomez, A. Kumar, N.
1316 Spassky, B.J. Mitchell, A. Meunier, and A.J. Holland. 2019b. Massive centriole production can

occur in the absence of deuterosomes in multiciliated cells. Nat. Cell Biol. 12:1544–1552. doi:10.1038/s41556-019-0427-x.

Meunier, A., and J. Azimzadeh. 2016. Multiciliated cells in animals. Cold Spring Harb. Perspect. Biol. 8:a028233. doi:10.1101/cshperspect.a028233.

Mir, L., M. Wright, and A. Moisand. 1984. Variations in the number of centrioles, the number of microtubule organizing centers 1 and the percentage of mitotic abnormalities in Physarum polycephalum amoebae. Protoplasma. 120:20–35. doi: 10.1007/BF01287614.

Mizukami, I., and J. Gall. 1966. Centriole replication. II. Sperm formation in the fern, Marsilea, and the cycad, Zamia. J. Cell Biol. 29:97–111. doi:10.1083/jcb.29.1.97.

Montenegro Gouveia, S., S. Zitouni, D. Kong, P. Duarte, B. Ferreira Gomes, A.L. Sousa, E.M. Tranfield, A. Hyman, J. Loncarek, and M. Bettencourt-Dias. 2018. PLK4 is a microtubule-associated protein that self-assembles promoting de novo MTOC formation. J. Cell Sci. 132. doi:10.1242/jcs.219501.

Moyer, T.C., K.M. Clutario, B.G. Lambrus, V. Daggubati, and A.J. Holland. 2015. Binding of STIL to Plk4 activates kinase activity to promote centriole assembly. J. Cell Biol. 209:863–878. doi:10.1083/jcb.201502088.

Nabais, C., S.G. Pereira, and M. Bettencourt-Dias. 2018. Noncanonical Biogenesis of Centrioles and Basal Bodies. Cold Spring Harb. Symp. Quant. Biol. 82:123–135. doi:10.1101/sqb.2017.82.034694.

Nakazawa, Y., M. Hiraki, R. Kamiya, and M. Hirono. 2007. SAS-6 is a Cartwheel Protein that Establishes the 9-Fold Symmetry of the Centriole. Curr. Biol. 17:2169–2174. doi:10.1016/j.cub.2007.11.046.

Nigg, E.A., and A.J. Holland. 2018. Once and only once: mechanisms of centriole duplication and their deregulation in disease. Nat. Rev. Mol. Cell Biol. doi:10.1038/nrm.2017.127.

Park, J.E., L. Zhang, J.K. Bang, T. Andresson, F. Di Maio, and K.S. Lee. 2019. Phase separation of Polo-like kinase 4 by autoactivation and clustering drives centriole biogenesis. Nat. Commun. 10. doi:10.1038/s41467-019-12619-2.

Peel, N., N.R. Stevens, R. Basto, and J.W. Raff. 2007. Overexpressing centriole-replication proteins in vivo induces centriole overduplication and de novo formation. Curr. Biol. 17:834–843. doi:10.1016/j.cub.2007.04.036.

Pelletier, L., O. Nurhan, E. Hannak, C. Cowan, B. Habermann, M. Ruer, T. Mu, and A.A. Hyman. 2004. The Caenorhabditis elegans Centrosomal Protein SPD-2 Is Required for both Pericentriolar Material Recruitment and Centriole Duplication. Curr. Biol. 14:863–873. doi:10.1016/j.

1350 Pimenta-Marques, A., I. Bento, C.A.M. Lopes, P. Duarte, S.C. Jana, and M. Bettencourt-Dias.
1351 2016. A mechanism for the elimination of the female gamete centrosome in Drosophila
1352 melanogaster. Science. 353:aaf4866. doi:10.1126/science.aaf4866.

1353 Port, F., H.M. Chen, T. Lee, and S.L. Bullock. 2014. Optimized CRISPR/Cas tools for efficient
1354 germline and somatic genome engineering in Drosophila. Proc. Natl. Acad. Sci. U. S. A.
1355 doi:10.1073/pnas.1405500111.

1356 Rale, M.J., R.S. Kadzik, and S. Petry. 2018. Phase Transitioning the Centrosome into a
1357 Microtubule Nucleator. Biochemistry. 57:30–37. doi:10.1021/acs.biochem.7b01064.

1358 Renzaglia, K.S., and D.J. Garbary. 2001. Motile Gametes of Land Plants: Diversity, Development,
1359 and Evolution. CRC. Crit. Rev. Plant Sci. 20:107–213. doi:10.1080/20013591099209.

1360 Riparbelli, M.G., and G. Callaini. 2003. Drosophila parthenogenesis: A model for de novo
1361 centrosome assembly. Dev. Biol. 260:298–313. doi:10.1016/S0012-1606(03)00243-4.

1362 Riparbelli, M.G., and G. Callaini. 2005. The meiotic spindle of the Drosophila oocyte: the role of
1363 Centrosomin and the central aster. J. Cell Sci. 118:2827–2836. doi:10.1242/jcs.02413.

1364 Riparbelli, M.G., D. Tagu, J. Bonhomme, and G. Callaini. 2005. Aster self-organization at meiosis:
1365 a conserved mechanism in insect parthenogenesis ? Dev. Biol. 278:220–230.
1366 doi:10.1016/j.ydbio.2004.11.009.

1367 Riparbelli, M.G., R. Stouthamer, R. Dallai, and G. Callaini. 1998. Microtubule Organization during
1368 the Early Development of the Parthenogenetic Egg of the Hymenopteran Muscidifurax uniraptor.
1369 Dev. Biol. 195:89–99. doi:10.1006/dbio.1997.8841.

1370 Rodrigues-martins, A., M. Riparbelli, G. Callaini, D.M. Glover, and M. Bettencourt-Dias. 2008.
1371 From centriole biogenesis to cellular function: Centrioles are essential for cell division at critical
1372 developmental stages. Cell Cycle. 7:11–16. doi:10.4161/cc.7.1.5226.

1373 Rodrigues-Martins, A., M. Riparbelli, G. Callaini, D.M. Glover, and M. Bettencourt-Dias. 2007.
1374 Revisiting the role of the mother centriole in centriole biogenesis. Science. 316:1046–50.
1375 doi:10.1126/science.1142950.

1376 Santos, H.G. Dos, D. Abia, R. Janowski, G. Mortuza, M.G. Bertero, M. Boutin, N. Guarin, R.
1377 Mendez-Giraldez, A. Nunez, J.G. Pedrero, P. Redondo, M. Sanz, S. Speroni, F. Teichert, M.
1378 Bruix, J.M. Carazo, C. Gonzalez, J. Reina, J.M. Valpuesta, I. Vernos, J.C. Zabala, G. Montoya,
1379 M. Coll, U. Bastolla, and L. Serrano. 2013. Structure and Non-Structure of Centrosomal Proteins.
1380 PLoS One. 8:e62633. doi:10.1371/journal.pone.0062633.

1381 Schindelin, J., I. Arganda-Carreras, E. Frise, V. Kaynig, M. Longair, T. Pietzsch, S. Preibisch, C.
1382 Rueden, S. Saalfeld, B. Schmid, J.Y. Tinevez, D.J. White, V. Hartenstein, K. Eliceiri, P.
1383 Tomancak1, and A. Cardona. 2012. Fiji - an Open Source platform for biological image analysis
1384 Johannes. Nat. Methods. 9. doi:10.1038/nmeth.2019.Fiji.

1385 Shohei, Y., and D. Kitagawa. 2018. Self-organization of Plk4 regulates symmetry breaking in
1386 centriole duplication. BioRxiv.

1387 Swaffer, M.P., A.W. Jones, H.R. Flynn, A.P. Snijders, and P. Nurse. 2016. CDK Substrate
1388 Phosphorylation and Ordering the Cell Cycle. Cell. 167:1750–1761.
1389 doi:10.1016/j.cell.2016.11.034.

1390 Takao, D., S. Yamamoto, and D. Kitagawa. 2019. A theory of centriole duplication based on self-
1391 organized spatial pattern formation. J. Cell Biol. 218:3537–3547.doi: 10.1083/jcb.201904156.

1392 Tavosanis, G., S. Llamazares, G. Goulielmos, and C. Gonzalez. 1997. Essential role for γ -tubulin
1393 in the acentriolar female meiotic spindle of Drosophila. EMBO J. 16:1809–1819. doi:
1394 10.1093/emboj/16.8.1809.

1395 Telley, I. a, I. Gáspár, A. Ephrussi, and T. Surrey. 2013. A single Drosophila embryo extract for
1396 the study of mitosis ex vivo. Nat. Protoc. 8:310–24. doi:10.1038/nprot.2013.003.

1397 Tram, U., and W. Sullivan. 2000. Reciprocal inheritance of centrosomes in the parthenogenetic
1398 Hymenopteran Nasonia vitripennis. Curr. Biol. 10:1413–1419. doi:10.1016/S0960-
1399 9822(00)00795-8.

1400 Tsuchiya, Y., S. Yoshiba, A. Gupta, K. Watanabe, and D. Kitagawa. 2016. Cep295 is a conserved
1401 scaffold protein required for generation of a bona fide mother centriole. Nat. Commun. 7:1–13.
1402 doi:10.1038/ncomms12567.

1403 Tyson, J.J., and B. Novak. 2001. Regulation of the Eukaryotic Cell Cycle: Molecular Antagonism,
1404 Hysteresis, and Irreversible Transitions. J. Theor. Biol. 210:249–263. doi:10.1006/jtbi.2001.2293.

1405 Uetake, Y., J. Loncarek, J.J. Nordberg, C.N. English, S. La Terra, A. Khodjakov, and G. Sluder.
1406 2007. Cell cycle progression and de novo centriole assembly after centrosomal removal in
1407 untransformed human cells. J. Cell Biol. 176:173–182. doi:10.1083/jcb.200607073.

1408 Vardy, L., and T.L. Orr-Weaver. 2007. The Drosophila PNG Kinase Complex Regulates the
1409 Translation of Cyclin B. Dev. Cell. 12:157–166. doi:10.1016/j.devcel.2006.10.017.

1410 Varmark, H., S. Llamazares, E. Rebollo, B. Lange, J. Reina, H. Schwarz, and C. Gonzalez. 2007.
1411 Asterless Is a Centriolar Protein Required for Centrosome Function and Embryo Development in
1412 Drosophila. Curr. Biol. 17:1735–1745. doi:10.1016/j.cub.2007.09.031.

1413 Wang, W.J., R.K. Soni, K. Uryu, and M.F.B. Tsou. 2011. The conversion of centrioles to
1414 centrosomes: essential coupling of duplication with segregation. J. Cell Biol. 193:727–739.
1415 doi:10.1083/jcb.201101109.

1416 Wong, Y.L., J. V Anzola, R.L. Davis, M. Yoon, A. Motamedi, A. Kroll, C.P. Seo, J.E. Hsia, S.K.
1417 Kim, J.W. Mitchell, J. Brian, A. Desai, T.C. Gahman, A.K. Shiau, and K. Oegema. 2015.
1418 Reversible centriole depletion with an inhibitor of Polo-like kinase 4. Science. 348:1155–1160.
1419 doi:10.1126/science.aaa5111.

1420 Yamamoto, S., and D. Kitagawa. 2019. Self-organization of Plk4 regulates symmetry breaking in
1421 centriole duplication. Nat. Commun. 10. doi:10.1038/s41467-019-09847-x.

1422 Yatsu, N. 1905. The formation of centrosomes in enucleated egg-fragments. J. Exp. Zool. 2.
1423 doi:10.1002/jez.1400020206.

1424 Zhao, H., Q. Chen, C. Fang, Q. Huang, J. Zhou, X. Yan, and X. Zhu. 2019. Parental centrioles
1425 are dispensable for deuterosome formation and function during basal body amplification. EMBO
1426 Rep. 20. doi:10.15252/embr.201846735.

1427 Zitouni, S., M.E. Francia, F. Leal, S.M. Gouveia, C. Nabais, P. Duarte, S. Gilberto, D. Brito, T.
1428 Moyer, M. Ohta, D. Kitagawa, A.J. Holland, E. Karsenti, T. Lorca, M. Lince-Faria, and M.
1429 Bettencourt-Dias. 2016. CDK1 prevents unscheduled PLK4-STIL complex assembly in centriole
1430 biogenesis. Curr. Biol. 26:1127–1137. doi:10.1016/j.cub.2016.03.055.

FIGURE 1

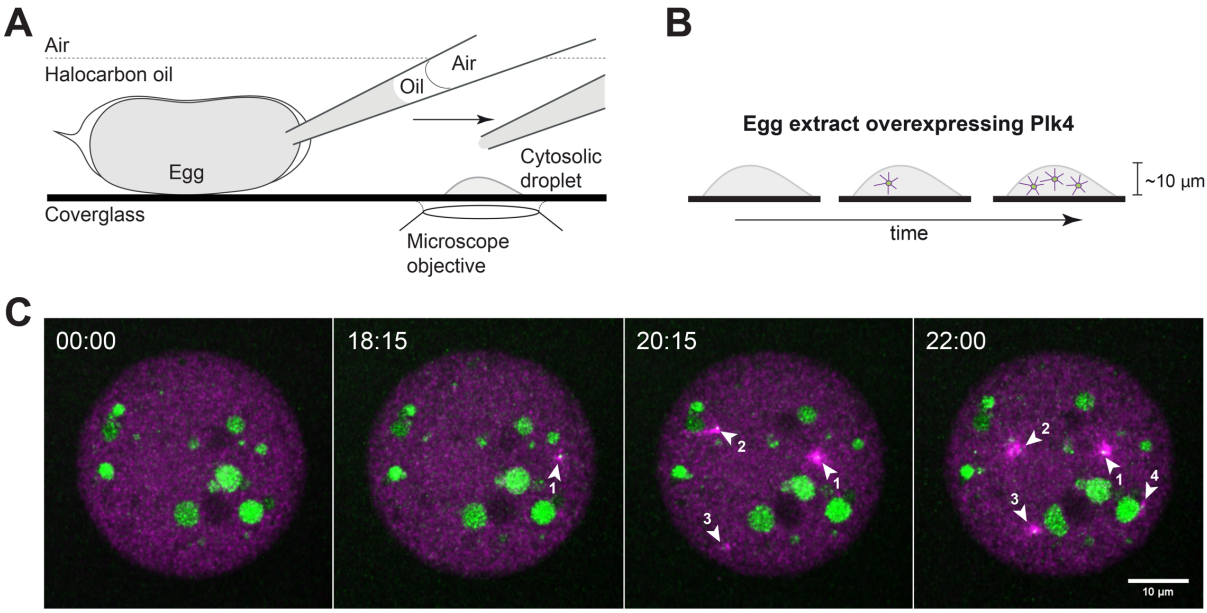

Figure 1: Visualisation of centrosome biogenesis in *Drosophila* egg extract. (A) *Drosophila* egg extract is prepared by rupturing the membrane and aspirating the cytoplasm with a micropipette. The content is deposited as a droplet on functionalised glass surface. **(B)** Each explant is followed by 3-dimensional time-lapse imaging, documenting centriole formation over time. **(C)** Z-projections from a time-lapse of a droplet of cytosolic extract isolated from a *Drosophila* egg overexpressing Plk4. Centrioles are absent in the first time point and form de novo throughout the experiment detected as spots (Spd2, in green) associated with a microtubule array (magenta) [arrowheads, numbers indicate the order of birth], reported by the microtubule associated protein Jupiter. The larger green blobs result from yolk autofluorescence. Time is reported as min:sec.

FIGURE 2

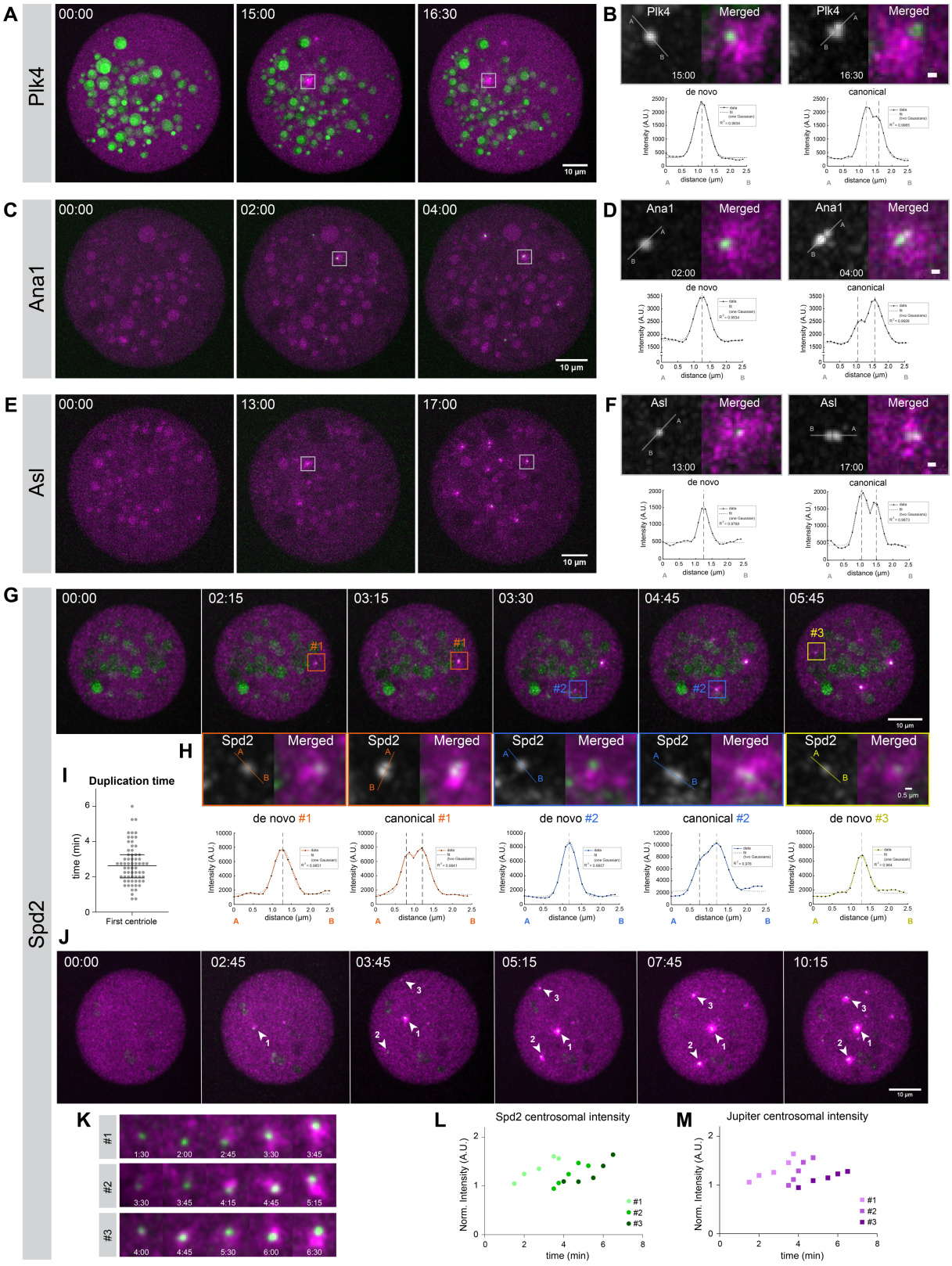

Figure 2: Centrioles assemble de novo, mature and duplicate within the same explants, in the absence of cell-cycle progression. Images show Z-projections from time-lapse movies of cytoplasmic explants extracted from non-cycling unfertilised eggs overexpressing Plk4. Newly assembled centrosomes load Plk4 **(A, B)**, Ana1 **(C, D)**, Asterless (Asl) **(E, F)** and Spd2 **(G, H, J)** shown in green

and nucleate microtubules as reported by the microtubule-associated protein Jupiter (magenta). The larger green blobs result from yolk autofluorescence, highly noticeable in the Plk4 and Spd2 panels. **(B, D, F)** Centrioles formed de novo also duplicate, which was inferred from changes in the intensity profile across the centrosomal signal (bottom plots); from a symmetrical Gaussian curve to a Gaussian mixture, suggesting the presence of more than one diffraction-limited structure (centriole). A uni- or bimodal Gaussian distribution was fitted to each “de novo” and “canonical” intensity profiles, respectively (dashed lines represent modes from fit). The coefficient of determination (R^2) is presented for each fit. Scale-bar in small insets = 0.5 µm. **(G)** Centrioles form de novo and canonically over time, therefore both biogenesis pathways co-occur. Centriole duplication was inferred from the change in the intensity profile across the Spd2 signal **(H**, bottom plots). Uni- or bimodal Gaussian fitting as in **B–F**. Colors represent one centrosome that first assembled de novo and later duplicated. **(I)** The duplication time depicted in the graph is the time elapsed between the documentation of the first centriole formed de novo (unimodal density) and the detection of a centriole pair (bimodal density). The horizontal line and error bars represent the median and interquartile range (N = 66 explants/eggs). **(K)** Insets of the first three centrosomes formed de novo in time-lapse **(J)** and their corresponding normalised and bleach-corrected intensity of Spd2 **(L)** and Jupiter reporting microtubules **(M)**, plotted over time. Time is reported in min:sec.

FIGURE 3

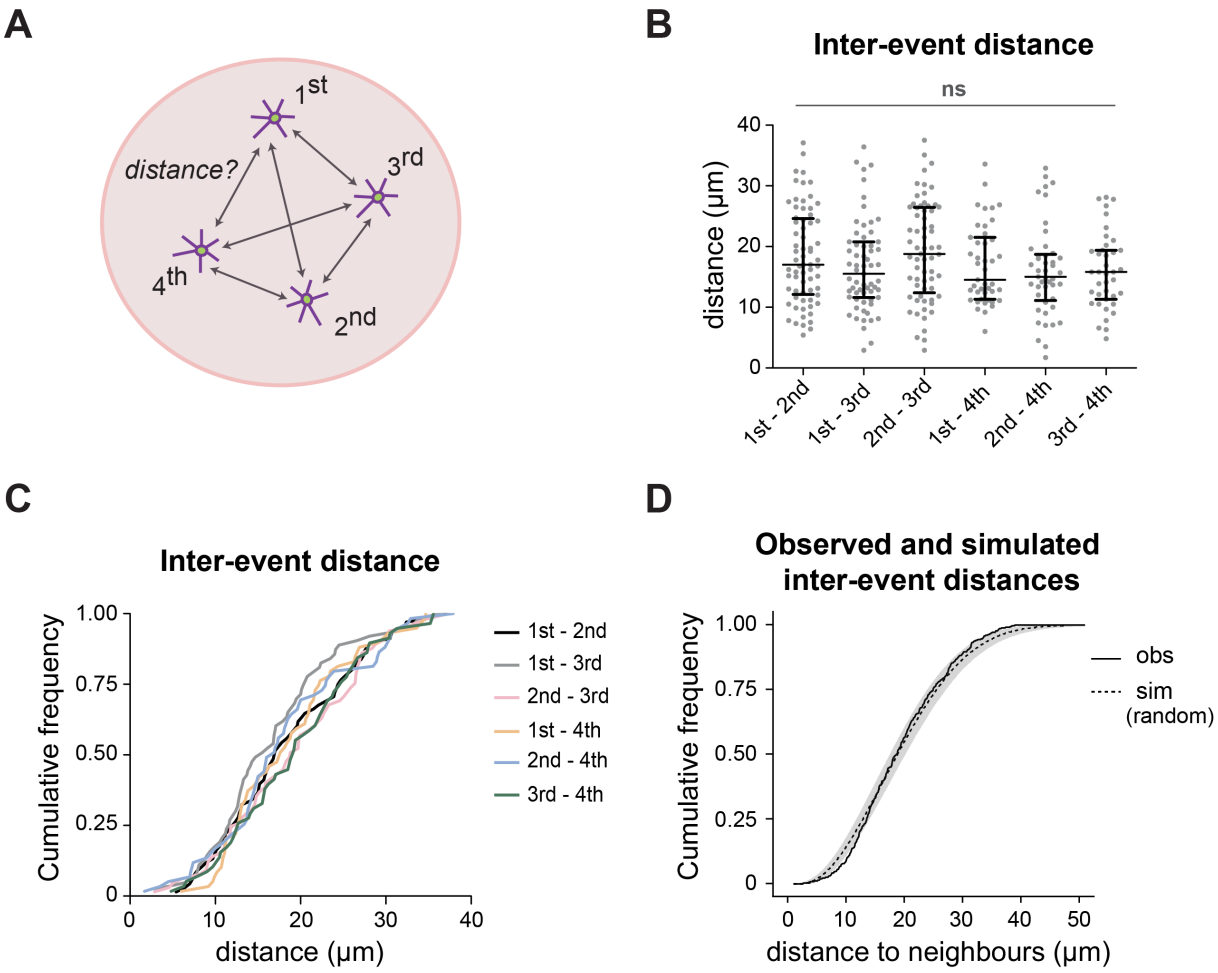

Figure 3: Spatial organisation of de novo centriole biogenesis. (A) Schematic representation of the experimental data analysis. The first four centrosomes formed de novo in the explants were tracked in 3D using the intensity signal from the Jupiter (MT reporter) channel (first tracking round) and Spd2 (centrosomal reporter) channel (second tracking round) combined. For each of the de novo birth events, an XYZT coordinate matrix was retrieved, from which the inter-event distances were calculated. Experimental N=68 droplets/eggs. Observed inter-event distances are plotted for all pairwise combinations of the first four de novo biogenesis events as a scatterplot **(B)** and as a Cumulative Distribution Function (CDF) **(C).** The horizontal lines and error bars in **(B),** represent the respective median and interquartile distance. No difference between mean inter-event distances (Kruskal-Wallis mean rank test, p-value= 0.467). **(D)** In silico simulations were performed to test if the observed experimental data deviates from a theoretical scenario in which all four birth events occurred at independent and identically distributed random positions with a uniform probability density distribution, within explants with similar geometry as in the experiments. Four random events were obtained in 100 simulations of 68 droplets. The graph depicts the median CDF of all experimentally observed (*obs*, solid line) and all simulated (*sim*, dashed line) inter-events distances, while the grey envelope indicates the 95% Confidence Interval (from quantile 0.025 to 0.975) for the simulated data. The experimental observations do not deviate from random simulations, suggesting that neighbour centrosomes do not influence the site where new centrosomes assemble de novo.

FIGURE 4

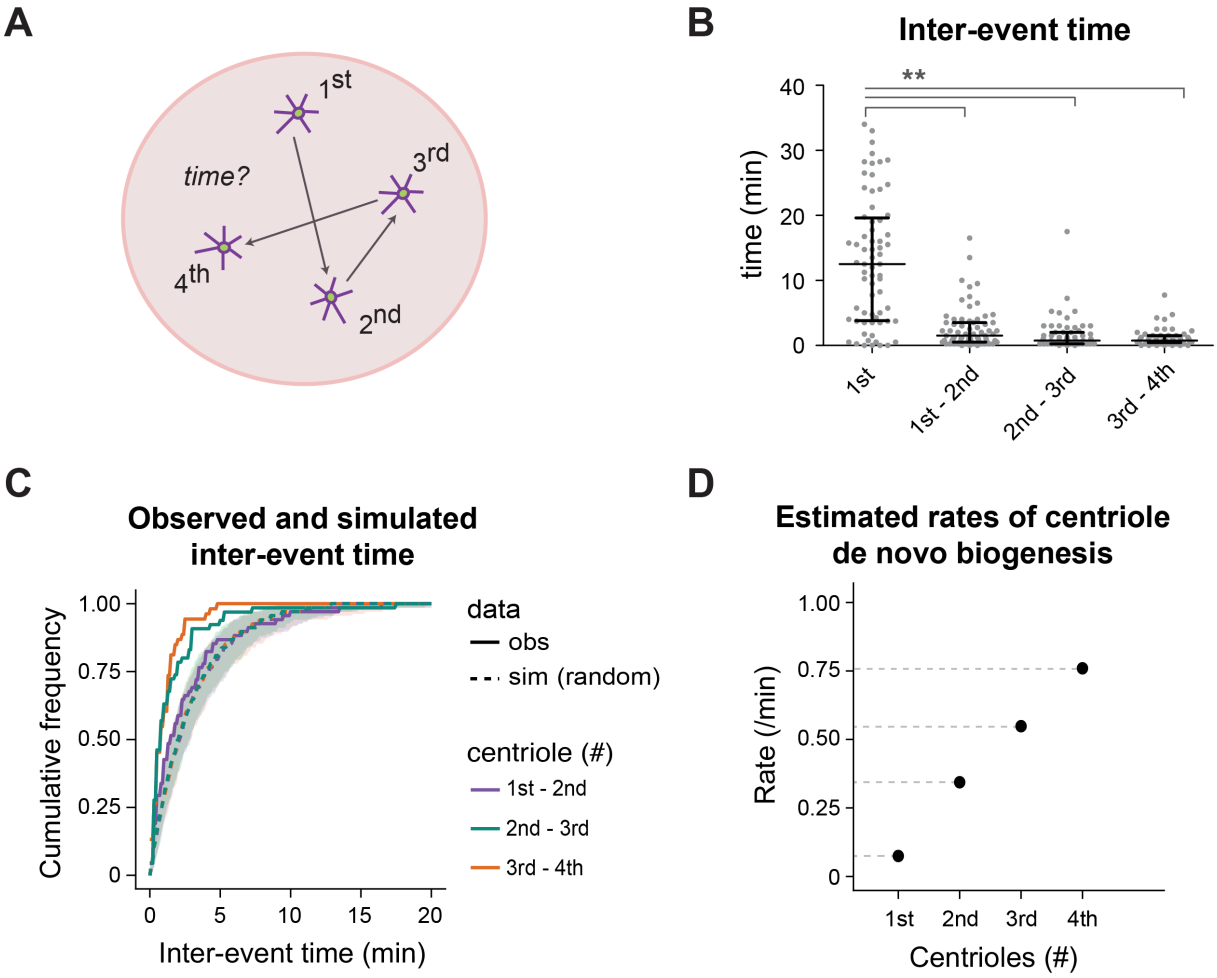

Figure 4: Temporal kinetics of de novo centriole biogenesis. (A) Schematic representation of the experimental data analysis. For each of the four de novo birth events, an XYZT coordinate matrix was retrieved, from which the inter-event time were calculated. Experimental N=68 droplets/eggs. Observed inter-event time between the first four de novo biogenesis events represented as a scatterplot **(B)** and as a Cumulative distribution function (CDF) **(C)**. The horizontal lines and error bars in **(B),** represent the respective median and interquartile range. The inter-event time is different between the first and subsequent events (Kruskal-Wallis mean rank test, p-value= 0.0047) **(C)** In silico simulations were performed to test if the observed experimental data deviates from a theoretical scenario where all four birth events occurred independently at a constant rate within an explant with similar geometry as in the experiments. Four random events were obtained in 100 simulations of 68 droplets. Due to the high uncertainty associated with the time of birth of the first event (i.e. it is not an absolute measurement since the initial time reference is arbitrary), the rate of birth used in the modelling was approximated to the inter-event time between the first and second events. The graph depicts the median CDF of the experimentally observed (*obs*, continuous line) and simulated (*sim*, dashed line) waiting times between the first and second, second and third and third and fourth events, while the grey envelope indicates the 95% Confidence Interval (from quantile 0.025 to 0.975) for the simulations. The observed and simulated waiting time distributions do not overlap, and differ more as centriole number increases, suggesting that

the rate of biogenesis is increasing over time. **(D)** Estimation of the experimental birth rates using Maximum Likelihood (MLE) fitting. An exponential distribution with rate $\lambda>0$ was fitted by MLE to the CDF of each observed waiting times. The estimated rate of de novo centriole assembly is represented in the graph as a function of the number of centrioles previously/already present in the volume.

FIGURE 5

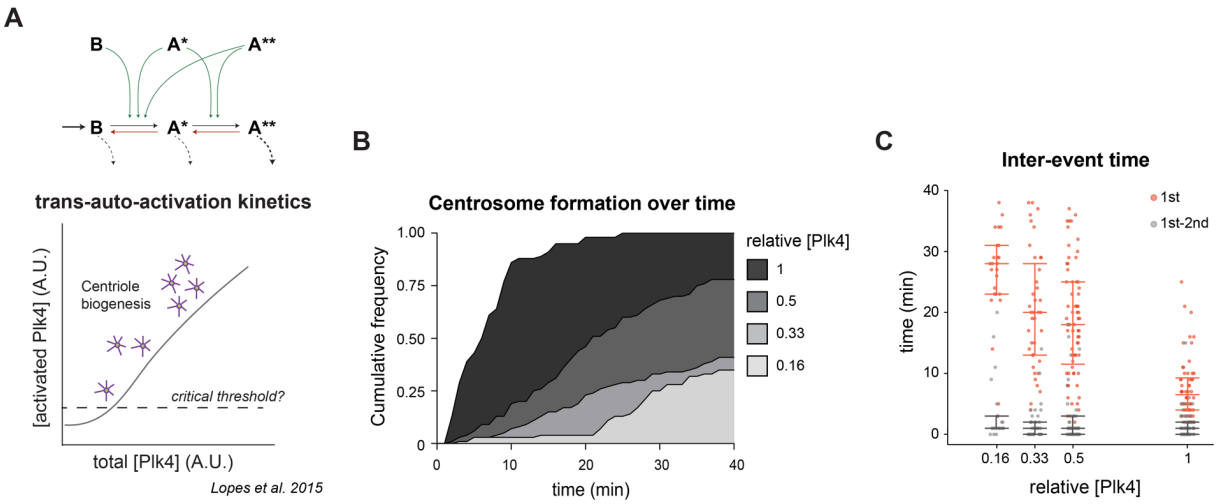

Figure 5: Plk4 concentration modulates the onset of centrosome biogenesis. (A) Model of Plk4 autoactivation and dephosphorylation. Plk4 trans-auto-phosphorylates to become fully active (Lopes et al. 2015), transitioning from an enzyme with basal activity – "B" form – to an activated form phosphorylated on its T-loop residue – "A*" form. Highly phosphorylated Plk4 – "A**" form – is also active but is targeted for degradation (Cunha-Ferreira et al., 2013; Guderian et al., 2010; Holland et al., 2012; Klebba et al., 2013). Dark arrows indicate the forward phosphorylation reaction flux, while red arrows indicate the reverse dephosphorylation flux catalysed by a putative counteracting phosphatase. The leftmost dark arrow marks the synthesised Plk4 that enters the system, while the dashed lines refer to Plk4 degradation. Green arrows depict the Plk4 forms that catalyse the forward flux. A non-linear balance between phosphorylation and dephosphorylation activities generates a Plk4 critical threshold, as a function of its concentration. Therefore, total concentration (active and inactive) of Plk4 in cells likely affects the timing at which a critical concentration is overcome and triggers centriole assembly. **(B)** Plk4 titrations were performed by mixing wild-type and Plk4 overexpressing eggs at different ratios. Time of onset of de novo centriole biogenesis is shown as cumulative distribution function for four relative concentrations of Plk4. Lower concentrations delay the initiation of de novo centriole biogenesis. **(C)** Time to the first de novo event, and inter-event time between the first and second de novo events in mixed explants with different concentrations of Plk4. In all dilutions tested, the time for the first event to occur is longer while the first to second inter-event time is unaffected. Median with interquartile range is presented for N=56, N=62, N=39 and N=25 explants at 1, 0.5, 0.33 and 0.16 relative concentration of Plk4, respectively.

FIGURE 6

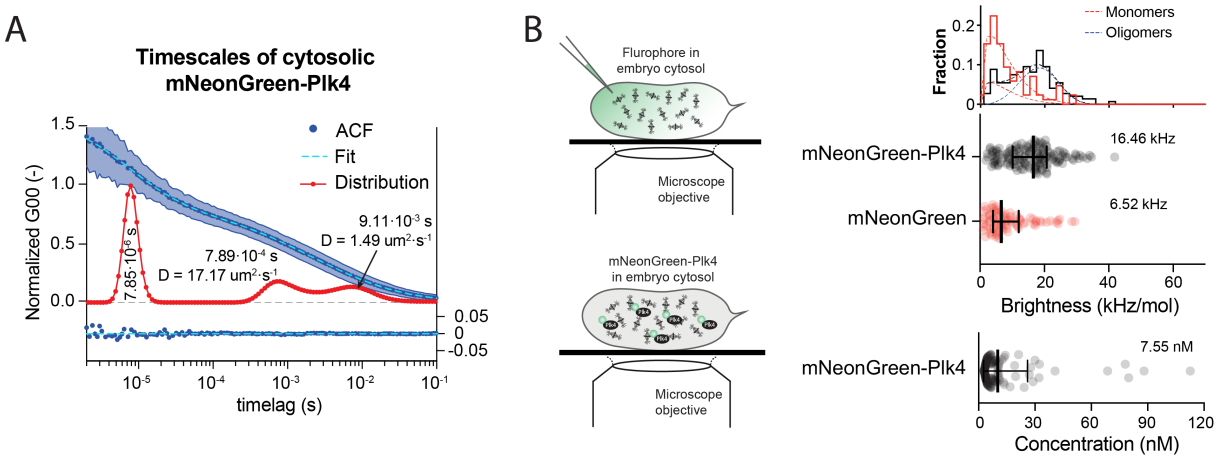

Figure 6: Single-molecule mNeonGreen-Plk4 quantifications in the cytosol of the syncytial fly embryo by Fluorescent Correlation Spectroscopy (FCS). (A) Normalised fitted Autocorrelation Function (ACF, "Fit" - light blue dashed line), with standard deviation (shaded area) and Maximum Entropy Method (MEM) distributions ("Distribution" – red line) for mNeonGreen-Plk4 in the cytoplasm. Based on the two fitting methods, three timescales were determined: the fastest timescale peak corresponds to the triplet state of the fluorophore ($7.85x10^{-6}$s); whereas the second and third slower timescales correspond to distinct 3D diffusional mobility of mNeonGreen-Plk4 in the cytoplasm, from which the diffusion coefficients (D) were calculated (fastest fraction: $7.89x10^{-4}$s, D=17.2 $\mu m^2/s$; slower fraction: $9.11x10^{-3}$s, D=1.49 $\mu m^2/s$). The residuals from the fitted data ("Fit") are shown below the graphs. **(B)** Plk4 undergoes limited oligomerisation in the cytosol of the *Drosophila* blastoderm embryo. The mNeonGreen distribution was fitted to a Weibull distribution, which has a peak value of 4100Hz. Next, the mNeonGreen-Plk4 data was fitted with an additional Weibull distribution (one for monomer-like and another for oligomer-like). The second mNeonGreen-Plk4 distribution peaks at 18450 Hz. From this analysis it follows that the overall normalised brightness (intensity per particle, mean ± SD) for mNeonGreen–Plk4 in the cytoplasm is higher than for the single mNeonGreen monomer injected into the cytoplasm at a similar concentration, indicating that Plk4 is present both as a monomer (around 30.1% of its diffusing pool) and as low-order oligomers (69.9% of diffusing mNeonGreen-Plk4 pool).

FIGURE 7

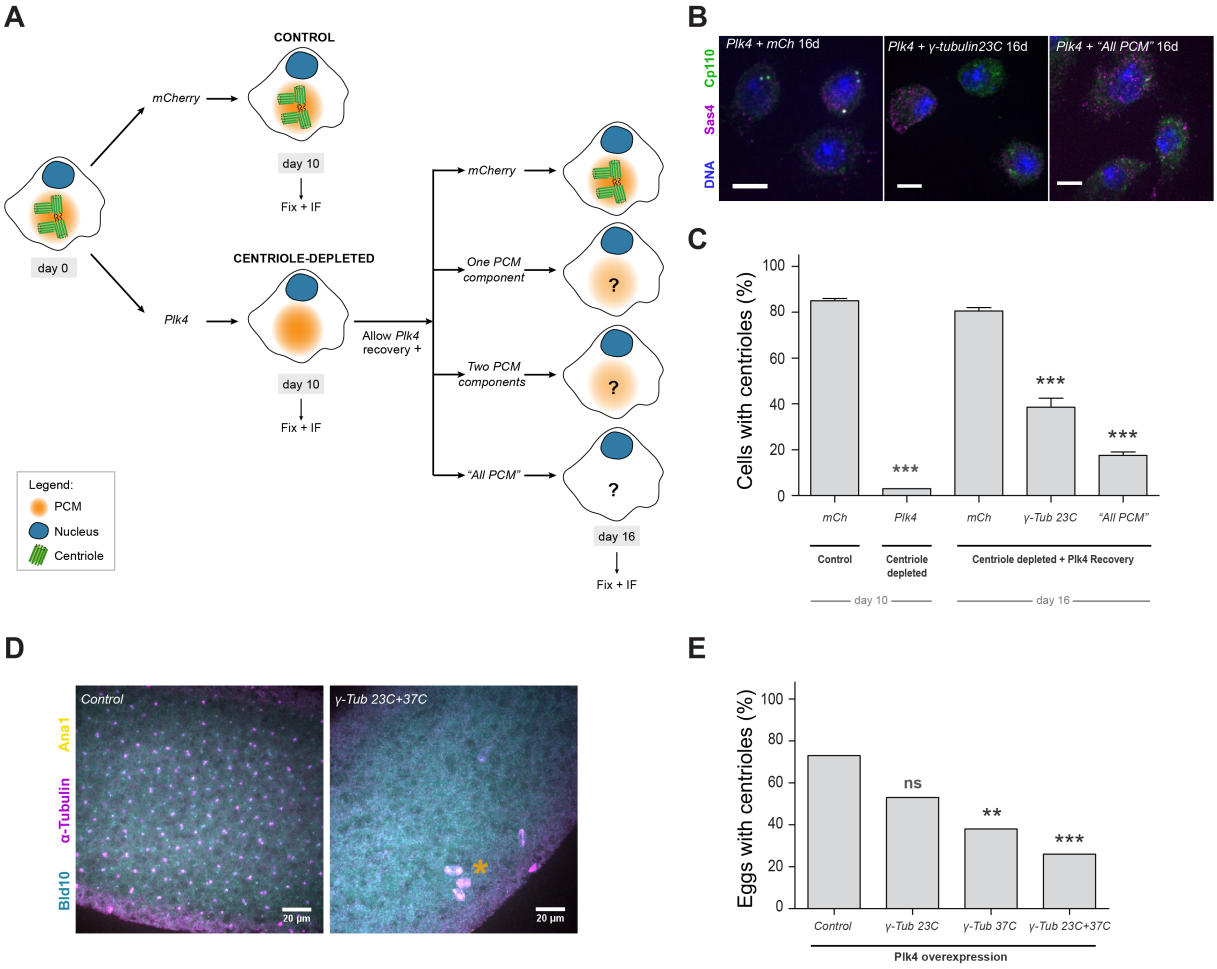

Figure 7: Centriole de novo biogenesis is partially impaired in PCM-depleted *Drosophila* cells. **(A)** DMEL cultured cells were treated with RNAi against Plk4 over the course of 12 days to deplete their centrioles. mCherry (mCh) RNAi was used as negative control. After 10 days, centriole-depleted cells were allowed to recover Plk4 translation while simultaneously depleting PCM components. **(B)** Z-projections of DMEL cells at day 16 treated with RNAi against mCherry (mCh), Gamma-tubulin 23C or "All PCM". Cells were stained with antibodies against Sas4 (magenta), Cp110 (green) and DAPI-stained (DNA, blue). Scale-bar = 5 µm. **(C)** Quantification of cells with centrioles after 10 and 16 days of RNAi treatment. Centriole number was scored in 300 cells per treatment, per independent experiment. Data is presented as average (with standard error of the mean - S.E.M.) of two independent experiments. Superscripts '*' denote statistical significance in treatments, where *, ** and *** indicate p< 0.05, 0.01, 0.001 (Pearson's χ^2 test and 2-proportions Z-test). **(D)** Z-projections of unfertilised eggs overexpressing Plk4 alone (Control) or in combination with RNAi against Gamma-tubulin 23C and 37C together. Eggs were stained with antibodies against Bld10 (cyan), Ana1 (yellow) and tyrosinated α-tubulin (magenta). Yellow asterisk highlights putative meiotic defects, previously described in oocytes from γ-tubulin 37C mutant females (Tavosanis et al. 1997). **(E)** Depletion of Gamma-tubulin 37C alone or together with Gamma-tubulin 23C impairs/limits de novo centriole biogenesis in unfertilised eggs overexpressing Plk4. Presence of centrioles was scored in eggs collected from virgin females aged for 4 hours. N=30

eggs (control); N=49 eggs (Gamma-tubulin 23C); N=47 eggs (Gamma-tubulin 37C); N=54 eggs (Gamma-tubulin 23C + 37C). **p< 0.01, Pearson's χ^2 test and 2-proportions Z-test.

SUPPLEMENTARY FIGURES

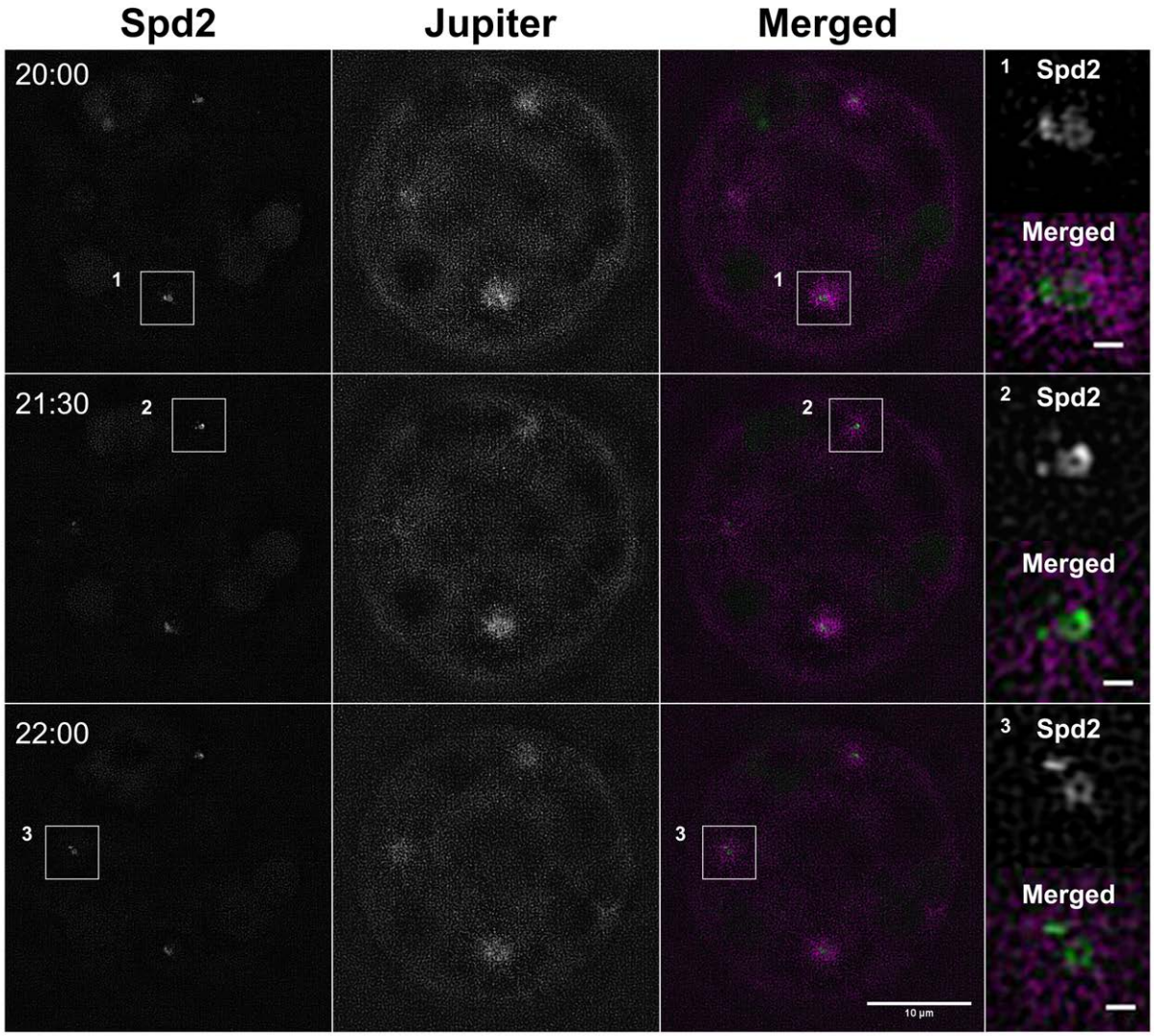

Supplementary Figure 1 (support to Figure 2): Visualisation of centrosome biogenesis in a *Drosophila* egg extract by 3D-Structured Illumination Microscopy (3D-SIM). Snapshots from a time-lapse acquisition of an unfertilised egg explant overexpressing Plk4. Centrioles (insets) are detected as barrel-shaped structures surrounded by the PCM component Spd2 (green) associated with a microtubule array (magenta), reported by the microtubule associated protein Jupiter. Insets depict three different centrosomes. Scale-bar = 0.5 µm. Centrioles formed de novo can duplicate. Time is reported as min:sec.

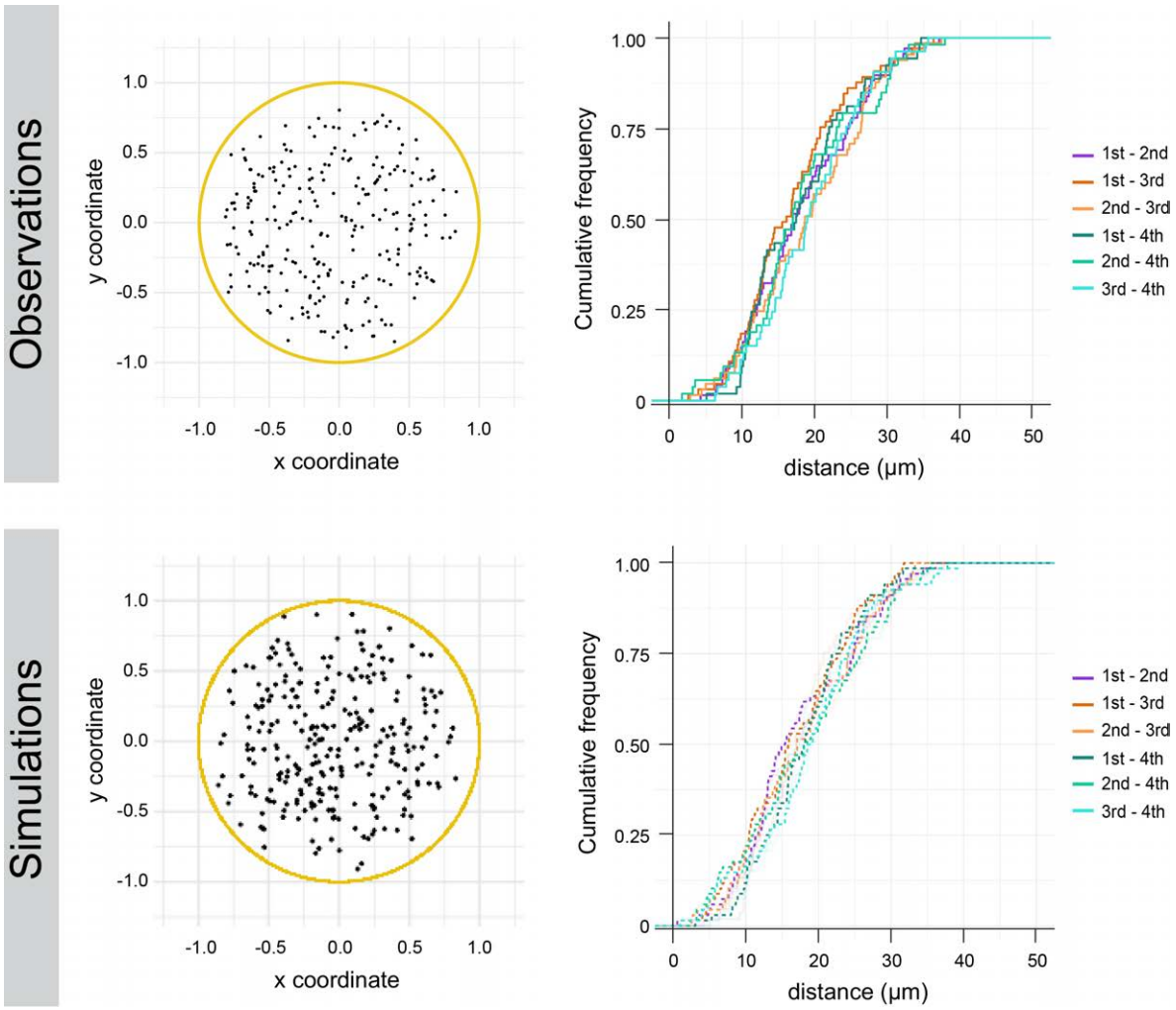

Supplementary Figure 2 (support to Figure 3): Spatial analysis of de novo centriole biogenesis in fly explants. Left: 2D Z-projections of the positions of centrioles at the moment they were first detected in the explants - 254 centrioles measured in 68 droplets ("Observations") and 272 centrioles from 68 simulated droplets ("Simulations"). All coordinates were normalised to the measured droplet diameter. **Right:** Distributions of observed and simulated inter-event distances measured in 3D for the first four centrosomes formed de novo in the explants.

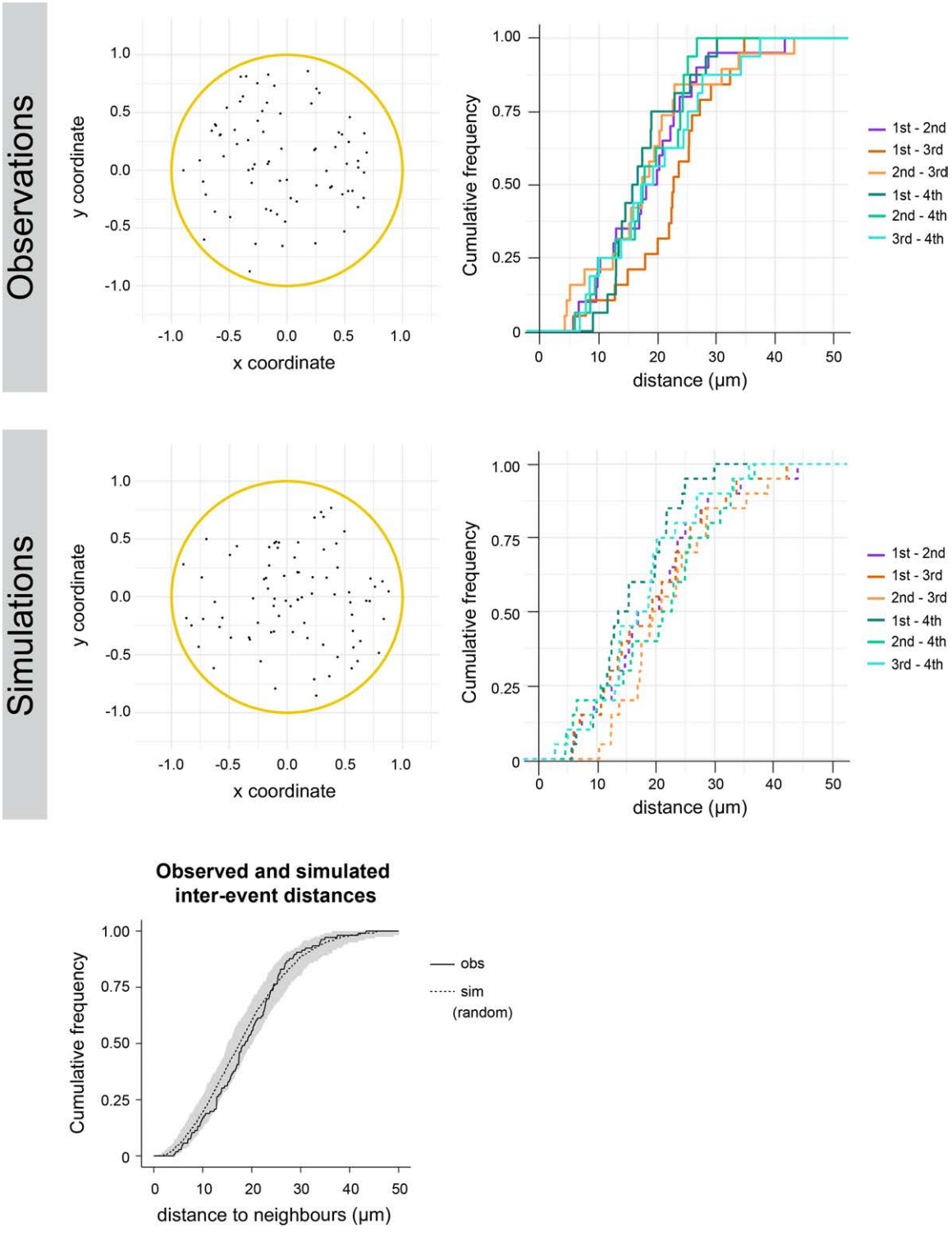

Supplementary Figure 3 (support to Figure 5): Spatial analysis of de novo centriole biogenesis in fly explants, at lower Plk4 concentration. Left: Z-projections of the positions of centrioles at the moment they were first detected in the explants - 75 centrioles measured in 20 droplets ("Observations") and 80 centrioles from 20 simulated droplets ("Simulations"). All coordinates were normalised to the measured droplet diameter. **Right:** Distributions of observed and simulated inter-event distances measured in 3D for the first four centrosomes formed de novo in the explants, at the lowest Plk4 overexpression ("0.16" relative concentration of Plk4). The grey envelope indicates the 95% Confidence Interval (from quantile 0.025 to 0.975) for the simulated data.

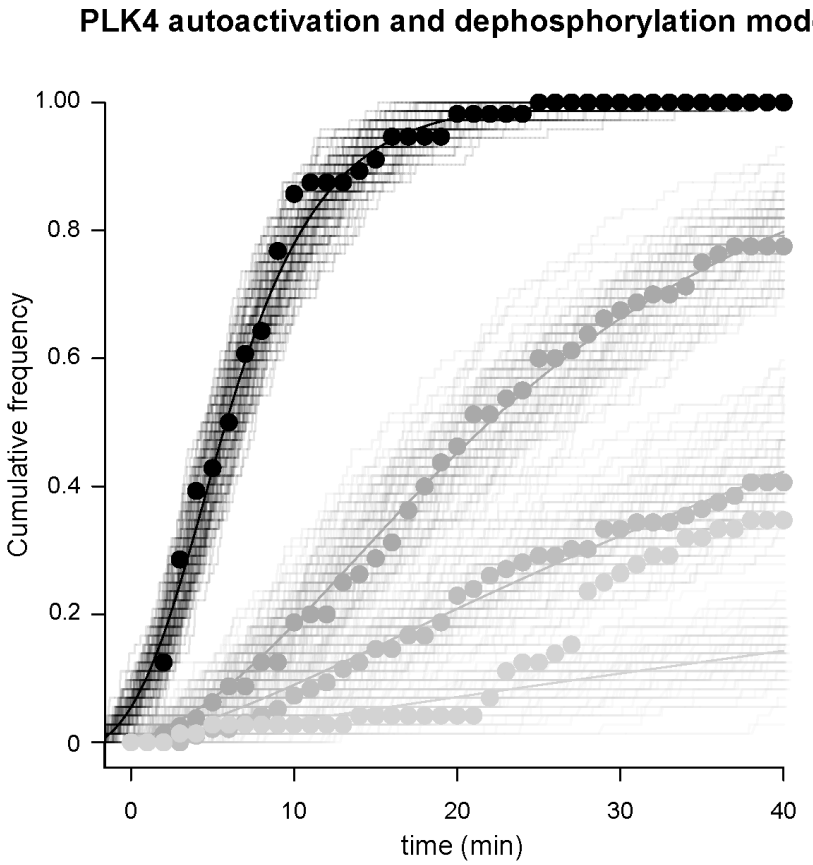

Supplementary Figure 4 (support to Figure 5): Fitting of Plk4 autoactivation and dephosphorylation model to data measured in explants at different Plk4 concentrations. The colour gradient represents different concentrations of Plk4. The different concentrations were prepared experimentally by mixing the cytoplasm from high overexpression eggs (taken as the unit "1", black) with cytoplasm from wild-type eggs, in different proportions such that the dilutions are "0.5", "0.33" and "0.16" relative concentrations. The dots are the relative frequency of explants containing at least one de novo formed centriole for the different concentrations of Plk4 ("1" (N = 56), "0.5" (N = 62), "0.33" (N = 39) and "0.16" (N = 25)). The lines are the solution of the model of Plk4 trans-autophosphorylation. The continuous lines are the solution of the ordinary differential equation model and the staircase lines are the results of stochastic simulations under the same parameter settings. The Plk4 activity in the High overexpression (denoted K) was adjusted, whereas the activities in the dilutions were set in relative terms (0.16K, 0.33K and 0.5K). The modelling and simulations, as well as the remaining parameters and values are described in section Statistics and mathematical modelling. Notice that as Plk4 concentration decreases, so does the number of droplets where centriole biogenesis occurs within 40 minutes of time-lapse recording

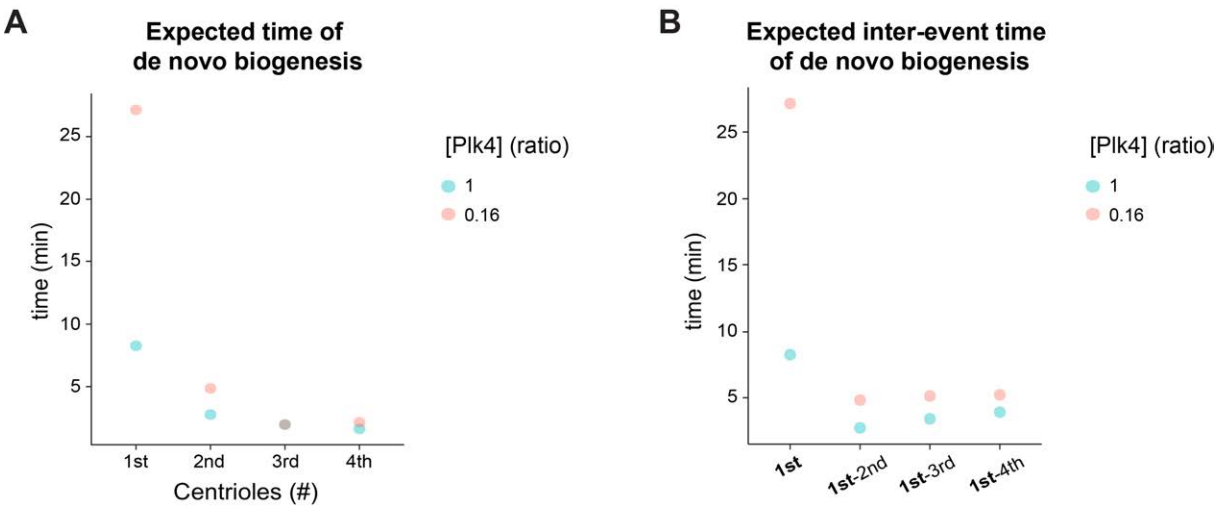

Supplementary Figure 5 (support to Figure 5): Temporal kinetics of de novo centriole biogenesis at different concentrations of Plk4. (A) Estimation of the mean centriole biogenesis times at high Plk4 overexpression ("1", in blue) and at the lowest Plk4 overexpression ("0.16", in orange) by ML estimation (MLE) fitting of a simple exponential model. **(B)** Estimation of the waiting time until the first de novo event and inter-event time between the first and subsequent de novo events, at high ("1", in blue) and the lowest ("0.16", in orange) overexpression of Plk4.

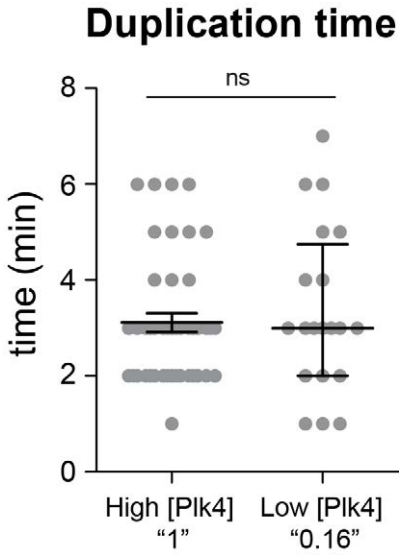

Supplementary Figure 6 (support to Figure 5): The duplication time of the first centriole formed de novo is similar at high ("1") and low Plk4 concentration ("0.16"). Centrioles formed de novo duplicate, on average, 3 min after their biogenesis, at both high ("1", N = 44 centrioles) and the lowest ("0.16" Plk4 Dilution, N = 20 centrioles) overexpression of Plk4. The horizontal lines and error bars represent the respective median and interquartile distance. The duplication time is not statistically different between the two conditions (Mann-Whitney test, p-value = 0.59).

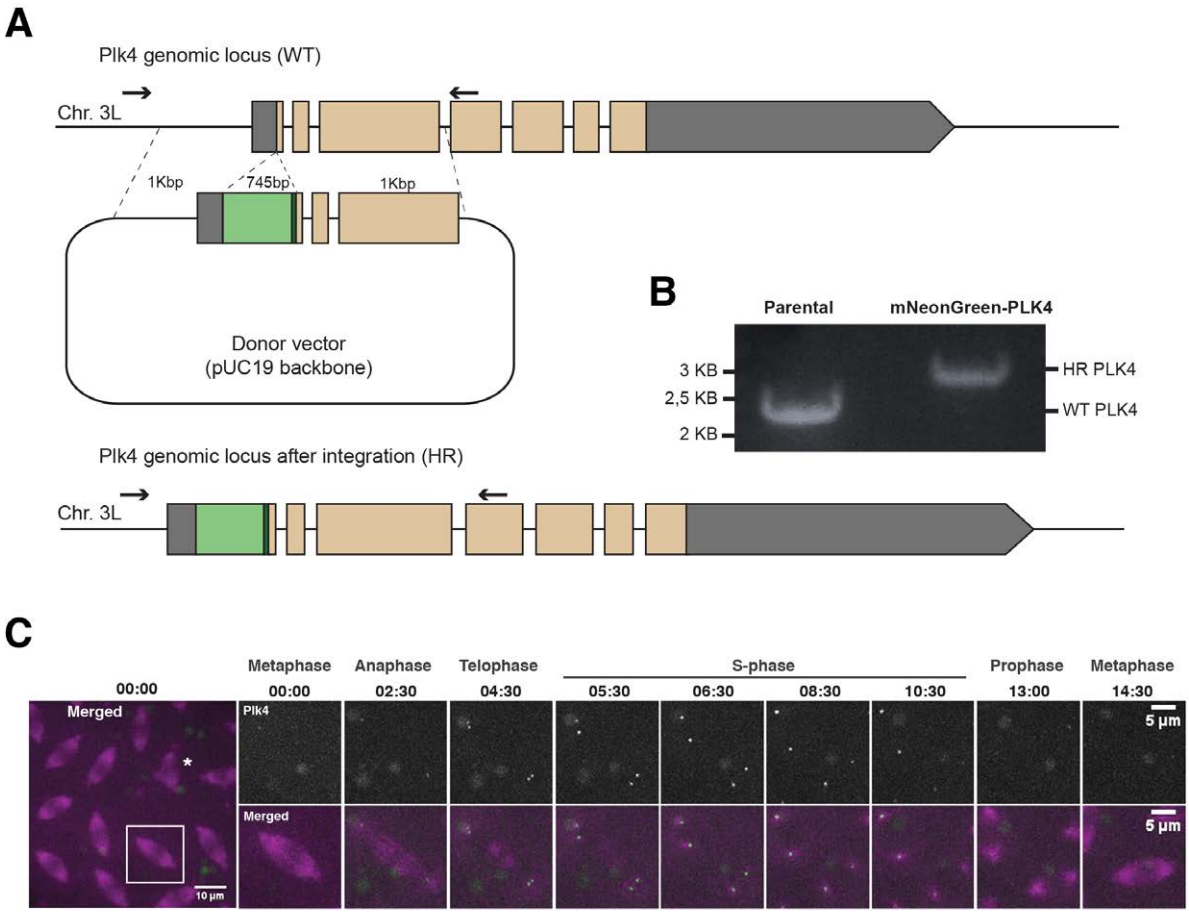

Supplementary Figure 7 (support to Figure 6): Insertion of a fluorescent tag into Drosophila Plk4 endogenous locus. (A) Schematic representation of the wild-type dmPlk4 locus (WT) and of the dmPlk4 locus after successful tag integration (HR). A donor plasmid carrying the mNeonGreen reporter and a small linker (dark green) flanked by 1 Kbp homology arms was used for homologous recombination. The UTRs are shown in grey and the coding sequences are depicted in orange. The arrows indicate the position of the screening primers dmPLK4 5UTR 3 FW and dmPLK4 1exon Rev, which are located outside the homology arms. **(B)** Integration of a fluorescent tag into Plk4 endogenous locus (HR Plk4) causes a migration shift of the PCR product in the agarose gel compared to the untagged Plk4 locus (WT Plk4). **(C)** Z- projection from a time-lapse video of a syncytial *D. melanogaster* embryo expressing endogenous mNeonGreen-Plk4 (green) and microtubule reporter RFP-**β**-tubulin (magenta). Plk4 localises at the centrosomes (high intensity tubulin spots) in interphase. Larger green dots result from yolk auto-fluorescence. At timepoint t=00:00 the embryo is in metaphase of nuclear cycle 11. The insets show the progression of a single nucleus and its daughters, throughout one cell-cycle. The cell-cycle stage is indicated above each image. Time is reported as min:sec. The asterisk indicates an abnormal mitotic spindle.

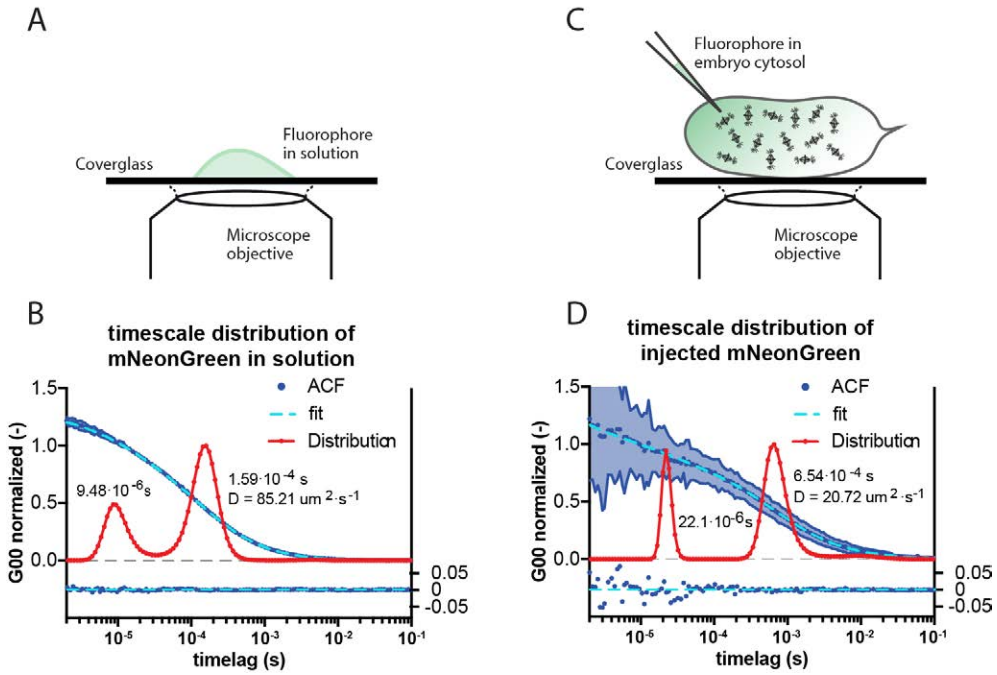

Supplementary Figure 8 (support to Figure 6): FCS measurements of purified mNeonGreen fluorophore. (A, B) Measurements of mNeonGreen in a buffer supporting viability of the cytoplasm (Telley et al 2013). **(C, D)** Measurements of mNeonGreen after injection into the cytosol of syncytial embryos expressing RFP-Tubulin. **(B, D)** show normalised fitted Autocorrelation Functions (ACF, blue dots and light-blue curve), with standard deviation (shaded area) and Maximum Entropy Method (MEM) Fit (red line). The time lags (diffusion times) determined using the two fitting methods shown next to the MEM-fit curves are in agreement. The peak at the fast timescale corresponds to the triplet state of the fluorophore ($9.48x10^{-6}$ s in solution; $22x10^{-6}$ s in the cytoplasm), whereas the second peak in the slower timescale corresponds to the 3D diffusion of mNeonGreen, from which a diffusion coefficient D was calculated ($1.59x10^{-4}$ s, D = 85.21 $\mu m^2/s$ in solution; $6.54x10^{-4}$ s, D = 20.72 $\mu m^2/s$ in the cytoplasm). The residuals obtained from the best fit are shown below the graphs.

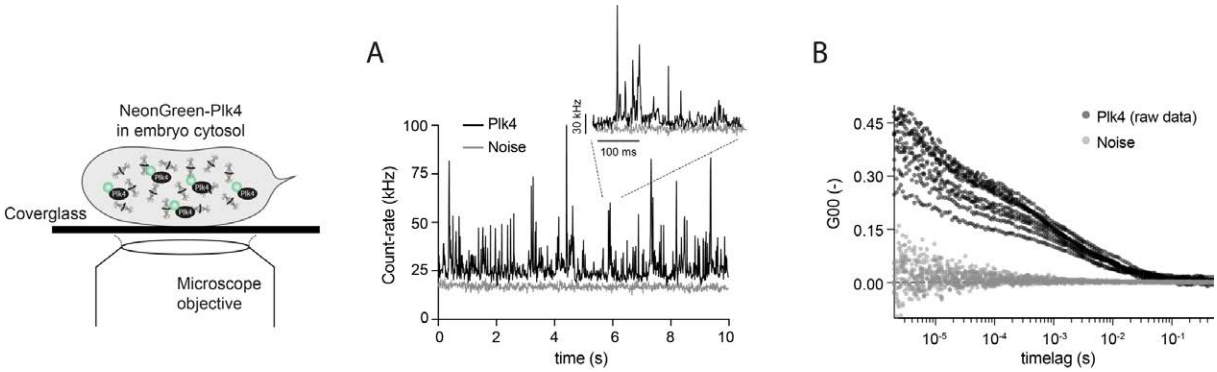

Supplementary Figure 9 (support to Figure 6): Single-molecule mNeonGreen–Plk4 quantifications in the cytosol of the syncytial fly embryo. (A) Intensity traces of mNeonGreen–Plk4 (black) and background noise (grey). Of note, intensity bursts of mNeonGreen–Plk4 are well distinguishable from background noise (inset). **(B)** Raw auto-correlation functions (ACF) from multiple independent FCS measurements. While the intensity of background acquisitions as measured in RFP–Tubulin expressing embryos does not autocorrelate, traces from mNeonGreen–Plk4 expressing embryos exhibit significant autocorrelation.

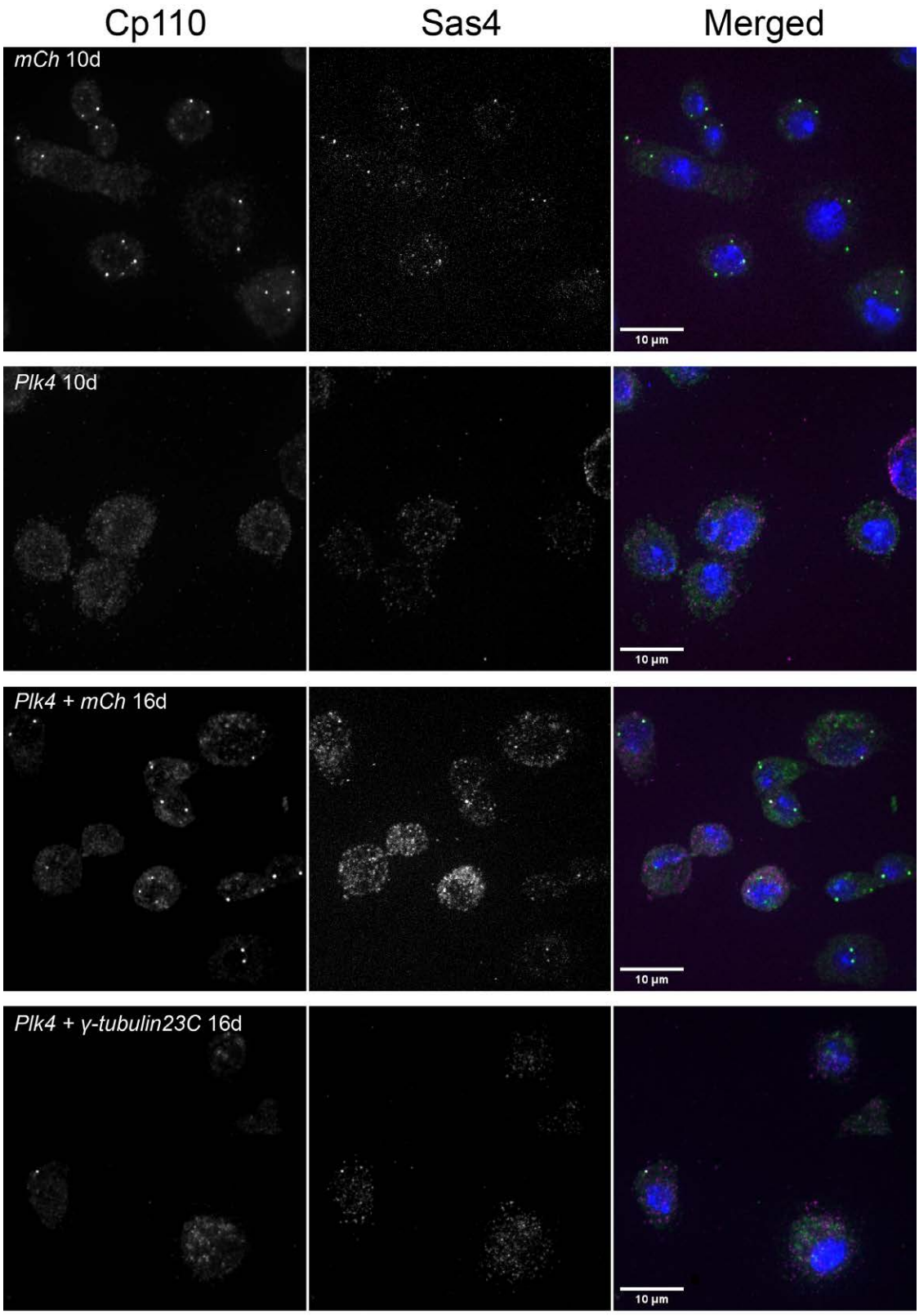

Supplementary Figure 10 (support to Figure 7): Centriole de novo biogenesis is partially impaired in PCM-depleted DMEL cells. (A) Z-projections of DMEL cells treated with RNAi against Plk4 or mCherry (mCh) for 10 days. Cells treated with RNAi against Plk4 gradually lose centrioles during

proliferation. After 10 days, centriole-depleted cells were allowed to recover Plk4 translation while simultaneously treated for four days with RNAi against individual PCM components – Cnn, Asl, D-Plp, Spd2 or **γ**-tubulin 23C – or combinations of two; some are specifically needed for PCM assembly in mitosis – Cnn and Spd2 (Conduit eLife 2014) – and during interphase – Cnn and D-Plp (Lerit JCB 2015). Additionally all four of these components – Cnn + Asl + D-Plp + Spd2 ("All PCM") were shown to be essential for PCM maintenance (Pimenta-Marques et al., 2016). The panels show centriole-depleted cells treated with RNAi against mCherry (recovering centriole normal number) and γ-tubulin 23C (abnormal centriole number). Cells were stained with centriolar markers Sas4 (magenta) and Cp110 (green); and DAPI-stained (DNA, in blue). **(B)** Quantification of centriole number per cell after 10 and 16 days of RNAi treatment. Data are the average of two independent experiments (with standard error of the mean - S.E.M.). Superscripts '*' denote statistical significance in treatments, where *, ** and *** indicate $p< 0.05$, 0.01, 0.001 (Pearson's χ^2 test and 2-proportions Z-test).

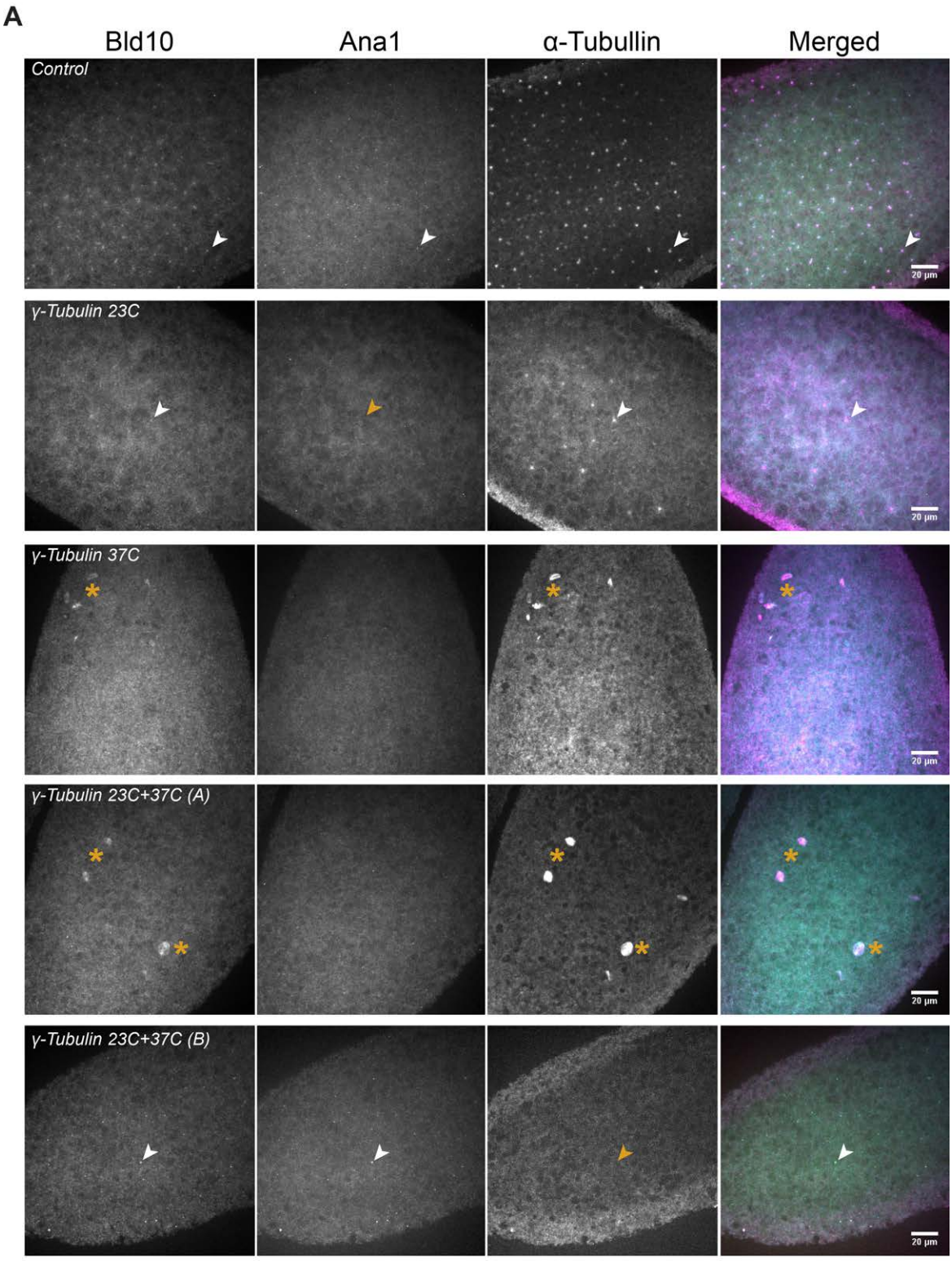

Supplementary Figure 11 (support to Figure 7): De novo centriole biogenesis is partially impaired in unfertilised eggs overexpressing Plk4 and depleted for Gamma-tubulin. (A) Z-projections of unfertilised eggs overexpressing Plk4 alone (Control) or together with RNAi against γ-tubulin 23C, γ-tubulin 37C or both. Eggs were stained with Bld10 (cyan), Ana1 (yellow) and tyrosinated α-tubulin (magenta). Centrioles (arrowheads) were identified by co-localisation of at least two of these markers. Yellow arrowheads depict centrioles for which one of the centrosomal proteins is not detected. Yellow asterisks reveal putative meiotic defects, previously described to occur in oocytes from γ-tubulin 37C mutant females (Tavosanis et al EMBO Journal 1997). **(B)** Quantification of unfertilised eggs with de novo centriole assembly driven by Plk4 overexpression and detected by the combination of two or three of either Bld10, Ana1 or tyrosinated α-tubulin. **p< 0.01, Pearson's χ^2 test and 2-proportions Z-test.

SUPPLEMENTARY TABLES

Supplementary Table 1: *D. melanogaster* strains generated and/or used in this study.

Allele	Source
mNeonGreen-Plk4 (endogenous)	This study
pUb-RFP- β2-Tubulin	Kitazawa et al., 2014
nanos-Cas9	Bloomington Drosophila Stock Center ID: 54591
V32-Gal4	Bloomington Drosophila Stock Center ID: 7062
pUASp-Plk4	Rodrigues-Martins et al., 2007
pUb-Spd2-GFP	homemade
(endo promoter) Ana1-tdTomato	Blachon et al., 2008
pUASp-GFP-Plk4	homemade
(endo promoter) Asl-mCherry	Conduit et al., 2015
Jupiter-GFP (endogenous)	Bloomington Drosophila Stock Center ID: 6836
Jupiter-mCherry (endogenous)	Lowe et al., 2014
pUASp-shRNA γ-Tubulin 23C	This study
pUASp-shRNA γ-Tubulin 37C	This study

Supplementary Table 2: List of oligonucleotides used for CRISPR-mediated knock-in of mNeonGreen into the endogenous *Drosophila melanogaster* Plk4 locus. The guide RNA (gRNA) was used to the target the genome editing at dmPlk4 N-terminus. The three combinations of primers were used to clone the donor vector with the mNeonGreen fluorescent reporter. A short flexible linker (highlighted in blue) was placed between the coding sequences of mNeonGreen and Plk4.

Construct name	Forward (5'-3')	Reverse (5'-3')
dmPLK4 gRNA	(sense) GTCGGCTAGCTATGTTATCCAAT	(antisense) AAACATTGGATAACATAGCTAGC
5' Homology Arm	CATATGCGAGGACACTTTCCAGCACTAC	GAATTCAGCTAGCCTTTTTTCTGTAGACTT ACTGAGCCACTTCGAATG
3' Homology Arm	GGTACCATGTTATCGAATCGAGCGTTTGG AGAAACAATTGAGG	GGATCCTAGAGTGAGATTCTACTAGC
mNeonGreen + linker	GAATTCATGGTGAGCAAGGGCGAGGAG	GGTACCGCCGGAGCCGCCGCCGCCGGA GCCGCCCTTGTACAGCTCGTCCATGC

Supplementary Table 3: Sequencing and screening primers used to check the mNeonGreen-Plk4 line generated in this study.

Oligo name	Sequence (5'-3')	Purpose
U6-3_seq_F2	GCTCACCTGTGATTGCTCC	sequencing the gRNAs cloned into pCFD3
dmPLK4 5UTR 1REV	CATTAGTGAAGATCATTAGCCAGC	sequencing the 5´UTR region of dmPlk4
dmPLK4 5UTR 1FW	CAAATATATTGGTGATAGTGCAGCCC	sequencing the 5´UTR region of dmPlk4
dmPLK4 5UTR 2 REV	CCGAAACAATGCCTAATGAGATATG	sequencing the 5´UTR region of dmPlk4
dmPLK4 5UTR 2 FW	GGGCTCAGCTTATTGTGGGATCGG	sequencing the 5´UTR region of dmPlk4
dmPLK4 5UTR 3 REV	GCTGGAAAGTGTCCTCGAAAATCC	sequencing the 5´UTR region of dmPlk4
dmPLK4 5UTR 3 FW	GGCGTAGAAGCTGATGGATAATTGC	Screening for positive insertions
dmPLK4 5UTR 4 REV	GCCGCAGTGTGCCGAACTTTTTCG	sequencing the 5´UTR region of dmPlk4
dmPLK4 5UTR 4 FW	GACGCCGAAGATGCCCAGACTATC	sequencing the 5´UTR region of dmPlk4
dmPLK4 5UTR 5 FW	CCCTCTTTATCGGGCTTGGCATCAAG	sequencing the 5´UTR region of dmPlk4
dmPLK4 (155-177) REV	ACGCGGTTAGTGAGTCCAGTGC	sequencing within the dmPlk4 gene
dmPLK4 F 501-521	TGAGCGCCATATGACCATGT	sequencing within the dmPlk4 gene
dmPLK4 (745-768) REV	GGCGGGCGTCCAACCAGCAGGGTG	sequencing within the dmPlk4 gene
dmPLK4 1exon Rev	GGAAGCACTTGTTGTGGTCCTGAG	Screening for positive insertions
dmPLK4 F 1000	AATTGCCTTATGAACAGACAGGT	sequencing within the dmPlk4 gene
Sak 5 exon R	ATCTCGTAGGCCATCCAATCTCTG	sequencing within the dmPlk4 gene
dmPLK4 F 1501-1521	AAAGTCACATACTTCAGTAC	sequencing within the dmPlk4 gene

Supplementary Table 4: FCS Parameters determined from the model-based fittings. Total number of measurements and embryos analysed and diffusion model applied to each experimental condition. According to the model, either one or two diffusion components were determined and their characteristic timescales and diffusion coefficients calculated. The fraction of each diffusing pool is presented as a percentage.

	No. of measurements/ No. of embryos	Diffusion model	timescale 1 (ms)	Diffusion coeff 1 ($\mu m^2/s$)	Fraction ofτD1 (%)	timescale 2 (ms)	Diffusion coeff 2 ($\mu m^2/s$)	Fraction ofτD2 (%)
mNeonGreen in solution	24	1 component 3D	0.15	85.2	100			
mNeonGreen in the cytosol	85 / 9	1 component anomalous 3D	0.65	20.7	100			
mNeonGreen-Plk4 in the cytosol	147 / 11	2 component 3D	0.79	17.2	52.3	9.11	1.49	47.7

Supplementary Table 5: List of primers used for dsRNA synthesis. The overhangs for in vitro transcription with the T7 RNA polymerase are depicted in blue.

Gene	Reference	CG No.	Forward Sequence (5' œ3')	Reverse Sequence (5´- 3')
mCherry	-	-	TAATACGACTCACTATAGGGAGAA TGGTGAGCAAGGG	TAATACGACTCACTATAGGGAGAGTT GACGTTGTAGG
Cnn	Pimenta-Marques et al., 2016	CG4832	TAATACGACTCACTATAGGGAGAA CCTCCAGGCGGCGGCAACT	TAATACGACTCACTATAGGGAGATGG CTCGAGCGGCATCCTT
Spd2	Pimenta-Marques et al., 2016	CG17286	TAATACGACTCACTATAGGGAGAG TCGCGTTCCAGCCAAGCAAAGA	TAATACGACTCACTATAGGGAGAAAT CCCCCACCTCCGTTAAGACTCAG
D-Plp	Pimenta-Marques et al., 2016	CG33957	TAATACGACTCACTATAGGGAGAG GAGCGCCTAAAGAACAGTG	TAATACGACTCACTATAGGGAGACTG ATCGAGCTGTTTGTGGA
Asl	Pimenta-Marques et al., 2016	CG2919	TAATACGACTCACTATAGGGAGAT TATGGTGAATGCCTTCGAC	TAATACGACTCACTATAGGGAGACTA GCTCAGCCTGCATGATG
Plk4	Rodrigues-Martins et al., 2007	CG7186	TAATACGACTCACTATAGGGAGAA TACGGGAGGAATTTAAGCAAGTC	TAATACGACTCACTATAGGGAGATTA TAACGCGTCGGAAGCAGTCT
γ-Tubulin 23C	Mahoney et al., 2006	CG3157	TAATACGACTCACTATAGGGGGTC ACAGATCGACTATCCTCC	TAATACGACTCACTATAGGGTTTTCT CATGACAGGCTACACG

Supplementary Table 6: Sequences of the oligonucleotides used to generate short hairpin RNA (shRNA) targeting different *Drosophila melanogaster* gene products. Each combination of oligos was annealed and cloned into pWALIUM22, to drive knock-down of each target gene specifically in the female germline.

Target gene	CG No.	Sense (5'-3')	Antisense (5'-3')	Landing site
γ-Tubulin 23C	CG3157	GGACGAGATCAGTGATGTAGT	ACTACATCACTGATCTCGTCC	attPZH-86Fb (3R)
γ-Tubulin 37C	CG17566	CGAAAGATTGCACATCCAAAC	GTTTGGATGTGCAATCTTTCG	attP2-68A4 (3L)

Supplementary Table 7: Lethality assay to determine viability of the shRNA fly lines. Number of pupae per vial in crosses between females carrying the V32-Gal4 and shRNA against **γ**-tubulin 37C and/or **γ**-tubulin 23C and w1118 males. V32-Gal4 females were crossed to w1118 males as control. For each genotype, four independent crosses were performed, with three technical repeats.

X ♂ w^{1118}	♀ V32-Gal4 (control)	♀ V32-Gal4; RNAi **γ**γ-tubulin 37C	♀ V32-Gal4; RNAi γ-tubulin 23C	♀ V32-Gal4; RNAi γ-tubulin 37C::γ-tubulin 23C
Cross #1	191/222/70	0/0/0	175/201/53	0/0/0
Cross #2	79/94/24	0/0/0	71/86/30	0/0/0
Cross #3	83/101/61	0/0/0	94/121/56	0/0/0
Cross #4	150/198/33	0/0/0	57/112/35	0/0/0

SUPPLEMENTARY TIME-LAPSE MOVIES

Movie 1 (support to Figure 1): Centriole biogenesis in a *Drosophila melanogaster* egg explant. Time-lapse movie of a droplet of cytosolic extract isolated from an unfertilised *Drosophila* egg overexpressing Plk4, acquired on a spinning-disk confocal microscope. The movie is a Z-projection. Centrioles are absent in the first time point and form de novo throughout the experiment detected as spots (Spd2, in green) associated with microtubule asters (magenta), reported by the microtubule associated protein Jupiter. Time (min:sec) is shown at the top left.

Movies 2A–D (support to Figure 2): Centrioles assemble de novo, recruit different centrosomal molecules and duplicate. Time-lapse movies of droplets of cytosolic extract from non-cycling unfertilised *Drosophila* eggs overexpressing Plk4, acquired on a spinning-disk confocal microscope. Videos are Z-projections showing centriole biogenesis reported by different centrosomal proteins in green – Plk4 (A), Ana1 (B), Asl (C) and Spd2 (D) – and the microtubule-associated protein Jupiter (magenta). The larger green blobs result from yolk autofluorescence, highly noticeable in the Plk4 movie. Time (min:sec) is shown at the top left of each 4 movie.

Movie 3 (support to Figure 6): mNeonGreen-Plk4 localisation in a syncytial *Drosophila* embryo. Time-lapse movie of an embryo expressing homozygous mNeonGreen-Plk4 (endogenously labeled by CRISPR, in green) and RFP-Tubulin (magenta), acquired on a spinning-disk confocal microscope, through nuclear cycles 10-13. The movie is a bleach-corrected intensity projection. Time (min:sec) is shown at the top left.